Cloud Radiative Forcing at the ARM Climate Research Facility: Part 1. Technique, Validation, and Comparison to Satellite-Derived Diagnostic Quantities.

Gerald G. Mace[1], Sally Benson[1], Karen L. Sonntag[1,2], Seiji Kato[3], Qilong Min[4], Patrick Minnis[5], Cynthia H. Twohy[6], Michael Poellot[7], Xiquan Dong[7], Charles Long[8], Qiuqing Zhang[1], David R. Doelling[9]

1. *Department of Meteorology, University of Utah*
2. *Cooperative Institute for Mesoscale Meteorological Studies University of Oklahoma, Norman, OK*
3. *Center for Atmospheric Sciences, Hampton University*
4. *State University of New York at Albany*
5. *NASA Langley Research Center*
6. *Oregon State University*
7. *University of North Dakota*
8. *Pacific Northwest National Laboratory*
9. *Analytical Services and Materials, Inc.*

Submitted to the Journal of Geophysical Research February, 2005

Corresponding Author Address:
Associate Professor Gerald G. Mace
201 S 1460 E Rm 819 (819 WBB)
Department of Meteorology
University of Utah
Salt Lake City, Utah 84112-0110
Email: mace@met.utah.edu
Telephone: 801 585 9489
Fax: 801 585 3681

Abstract: It has been hypothesized that continuous ground-based remote sensing measurements from active and passive remote sensors combined with regular soundings of the atmospheric thermodynamic structure can be combined to describe the effects of clouds on the clear sky radiation fluxes. We critically test that hypothesis in this paper and a companion paper (Part II). Using data collected at the Southern Great Plains (SGP) Atmospheric Radiation Measurement (ARM) site sponsored by the U.S. Department of Energy, we explore an analysis methodology that results in the characterization of the physical state of the atmospheric profile at time resolutions of five minutes and vertical resolutions of 90 m. The description includes thermodynamics and water vapor profile information derived by merging radiosonde soundings with ground-based data, and continues through specification of the cloud layer occurrence and microphysical and radiative properties derived from retrieval algorithms and parameterizations. The description of the atmospheric physical state includes a calculation of the infrared and clear and cloudy sky solar flux profiles. Validation of the methodology is provided by comparing the calculated fluxes with top of atmosphere (TOA) and surface flux measurements and by comparing the total column optical depths to independently derived estimates. We find over a 1-year period of comparison in overcast uniform skies, that the calculations are strongly correlated to measurements with biases in the flux quantities at the surface and TOA of less than 10% and median fractional errors ranging from 20% to as low as 2%. In the optical depth comparison for uniform overcast skies during the year 2000 where the optical depth varies over 3 orders of magnitude we find a mean positive bias of 46% with a median bias of less than 10% and a 0.89 correlation coefficient. The slope of the linear regression line for the optical depth

comparison is 0.86 with a normal deviation of 20% about this line. In addition to a case study where we examine the cloud radiative effects at the TOA, surface and atmosphere by a middle latitude synoptic-scale cyclone, we examine the cloud top pressure and optical depth retrievals of ISCCP and LBTM over a period of 1 year. Using overcast period from the year 2000, we find that the satellite algorithms tend to bias cloud tops into the middle troposphere and underestimate optical depth in high optical depth events (greater than 100) by as much as a factor of 2.

1. Introduction

The Atmospheric Radiation Measurement (ARM) program was initiated in the early 1990's with a goal of improving the parameterization of clouds in GCMs (Stokes and Schwartz, 1994; Ackerman and Stokes, 2003). A primary contribution of the ARM program has been to continuously document the vertical distribution of clouds, the associated thermodynamic states, and the effect of clouds on the surface radiation budget at a few highly instrumented sites. The ARM program began at about the time of several intensive field programs known as the First ISCCP Regional Experiments (FIRE) that were conducted in the late 1980's and the early 1990's (Randall et al, 1998). The case study approach of the FIRE deployments was fruitful in that a great deal was learned about the properties of cirrus and stratus clouds (Stephens, 1995; Randall, 1995). What was missing from these experiments was sufficient statistical breadth to determine how the knowledge gained from the case studies could be generally applied to the atmosphere in the form of GCM parameterizations. This difficulty was recognized, and the ARM planners speculated that a long-term field project could complement short-term intensive studies. While the ARM observational paradigm lacks the global nature of a satellite-based program, it is complementary in that the sheer continuity and breadth of the continuous multi-year ground-based data ensures that, given sufficient time, a statistically significant sample of the accessible climate states will be observed at a ground site – i.e. the ergodic hypothesis (Peixoto and Oort, 1993). The ARM dataset exists in a fairly raw form, however. Even though the data are continuously collected, quality controlled, routinely calibrated, and made freely available to the

scientific community, converting the observations into descriptions of cloud properties and radiative heating is a specific challenge that we address here.

In this paper, we describe a data analysis technique that attempts to reduce the raw ARM data into a meaningful description of the atmospheric physical state. Our motivation for pursuing this goal is the assumption that simultaneous knowledge of the cloud properties, and the large scale meteorology, along with their statistics, over extended time periods can lead to an improved understanding of the coupling between the resolved scale meteorology and the radiative feedbacks to the atmospheric circulation. In this paper and a companion paper (hereafter referred to as Part II) we examine the cloud radiative forcing of the atmosphere as a function of cloud type and the atmospheric synoptic state at the ARM Southern Great Plains (SGP) central facility (SCF) during the year 2000 with special emphasis on the month of March. Following Rossow and Zhang (1995; hereafter RZ95), The CRE is defined as the difference between the all sky and clear sky fluxes in units of watts per square meter (Wm^{-2}), while the CRF is defined as the actual heating rate or net cloud induced convergence of radiant energy into a volume (Webster and Stephens, 1984; Stephens, 2004). In the next section, we describe the data analysis procedure and validation of the results using TOA and surface cloud radiative observations. In section 3, we conduct a direct comparison of the cloud top pressure and total column optical depth with similar quantities produced by the International Satellite Cloud Climatology Product (ISCCP; Rossow and Zhang, 1999) and by an analysis of Geostationary Operational Environmental Satellite (GOES) data (Minnis et al, 1993, 1995). In Part II we consider the evolution of the synoptic scale atmosphere over the central U.S. during March 2000

and the coupling between the synoptic state, the cloud types, and the radiative feedbacks that were observed at the SCF and we examine the radiative feedbacks to the atmosphere as a function of cloud type.

2. Technique

We begin this section with a discussion of the data streams that are particularly important to our characterization of the atmospheric state, and then we describe a methodology to merge these raw individual data streams into a reasonably complete time dependent description of the atmospheric column over the SCF. During this discussion, we use for illustration the period from 1-3 March 2000 (Hereafter dates will be referred to using a month/day convention: i.e. 3/1-3/3). During this period a deep middle latitude cyclone passed over the SGP region. Figure 1 shows the evolution of the 500 mb height and vorticity field during this period beginning with a migratory ridge followed by a closed low that moved over the SGP from the southwestern U.S. Satellite imagery in Figure 2 shows that cirrus upstream of the 500 mb ridge on 3/1 gave way to a deep cloud system on 3/2 followed by a large area of boundary layer clouds with some higher clouds. This period marked the beginning of a multi-week intensive observational campaign at the SCF when multiple aircraft and several additional ground-based instruments were assembled to investigate the three dimensional properties of clouds that passed through the region.

The ARM data that we consider consist of measurements from several independently operating instruments situated in a cluster at the SCF. These instruments nominally operate on a continuous basis, the data streams go through separate routine calibration and quality control

procedures, and the data are eventually made freely available in an archive facility. Since the data are stored in a fairly raw form (temporally resolved files of geophysical measurements and metadata from particular instruments), the data are not immediately amenable, with a few exceptions, to describing the physical properties of the atmosphere. Remote sensors, for instance, are often sensitive to certain aspects of the atmosphere that may require interpretation. Radar, for instance, is sensitive to the sixth moment of the particle size distribution while the third moment is most descriptive of condensed mass and the second moment of optical extinction. Even lidar measurements, which are sensitive to the second moment are modulated by two-way extinction and multiple scattering. Our task is to combine the raw ARM data into a consistent entity that lends itself to describing the time evolving physical state of the column. While this task eventually reduces to estimating cloud microphysical and radiative properties, the initial data processing we undertake should be addressed briefly. See the Appendix for more detail.

The initial data processing has two essential goals. The first is to characterize the continuous thermodynamic state of the atmospheric column and the second is to use the active remote sensors to identify the locations of cloud. While ARM has devoted considerable resources to launching radiosondes from the SCF and from several boundary facilities, the record is not continuous. Only during IOPs are radiosondes launched at 3-hourly intervals 24 hours per day. At other times the schedule is less regular. Furthermore, other data sources such as continuous ground-based meteorological information and measurements of the water vapor path from the microwave radiometer are available. Therefore, we have developed a simple scheme to routinely combine available radiosondes with other more continuous measurements. For instance, the

water vapor profiles are always adjusted or scaled by the liquid water path derived from the MWR observations.

The MMCR data are also processed beginning with the raw reflectivity and Doppler moments. Because the MMCR cycles through several modes to optimize sensitivity taking a total of 36 seconds for one cycle, it is important that the data from the individual modes are carefully screened and then combined. We follow a technique similar to that described by Clothiaux et al. (1995) to identify significant return in the data. We then combine the cloud measurements with the thermodynamics on a height-time grid that has 90m and 5 minute resolution. For most variables such as the Doppler moments, averaging is performed in time. For quantities that are only defined in clouds (such as radar reflectivity), we average only those observations during a 5 minute period deemed to be associated with clouds by the cloud mask and we store the number of actual cloud occurrences in the 5 minute period along with the number of possible occurrences for later consideration. This 5 minute and 90 m time series forms the basis of what we term the column physical characterization (for convenience, we hereafter refer to this as the CPC). Additional details on the data reduction can be found in the Appendix.

Figures 3 and 4 show the microwave radiometer measurements and the thermodynamics derived for the case study period (3/1-3/3) while Figure 5 illustrates the MMCR data. We find that a highly variable layer of cirrus was observed by the MMCR beginning on the afternoon of 3/1 that appears to have passed over the radar in 4-5 distinct pulses. The layers deepened to be 3-4 km thick and were capped at the tropopause with each pulse lasting 2-3 hours followed by a 1-2 hour separation. Following the final cirrus episode, a deep cloud system that marked the

advancing middle latitude front and low pressure system was observed by the MMCR. Rain began at approximately 11 UTC on 3/2 and persisted until just after 20 UTC on 3/2 with a break in precipitation between 1630 and 1830 UTC. The precipitation periods as diagnosed from an empirical technique applied to microwave radiometer data (described in the appendix) is shown as a background light red on the radar height-time figure. Note that a radar bright band can be observed during this period of heavy cloud cover and precipitation. It is interesting to note the close correspondence between the radar time series and the features on the satellite imagery. Note that the radar shows no obvious signs of attenuation that would limit the detection range during this precipitation event since it records echo nearly to the tropopause.

The deep clouds that passed over the radar prior to 1630 UTC on 3/2 were followed by a transition to a layer of clouds based in the boundary layer with tops near 4 km with scattered cirrus that is plainly visible on the 1830 UTC 3/2 satellite image. The heavy clouds with rain that moved over the SCF after 1900 UTC on 3/2 can be seen as the region of colder topped cloud cover just southwest of the SCF in the 1830 UTC image. The cloud layer thinned considerably after 21 UTC and was predominantly a boundary layer cloud layer. While disturbances rotated around the vortex, the low pressure center passed just north of the SCF at around 12 UTC. One of these disturbances resulted in deeper clouds and a period light rain as it passed over the SCF between 6 and 9 UTC on 3/3. The cold sector of the cyclone brought occasional cirrus over a general boundary layer overcast during the day on 3/3. This period has been a focus of study since the NASA ER2 flew a mission under the newly launched Terra satellite that passed nearly overhead at 1735 UTC while the University of North Dakota Citation sampled the boundary layer clouds in situ (Dong and Mace, 2003; Dong et al., 2002).

2.2 Cloud Microphysical and Radiative Properties

The goal of creating a continuous record of cloud microphysics with ARM data has been longstanding but difficult to achieve. While algorithms have been developed to treat specific cloud types such as thin cirrus (Mace et al., 1998, 2002; Matrosov, 1994) and boundary layer liquid-phase clouds (Frisch et al., 1995, 1998; Mace and Sassen 2000; Dong and Mace 2003), developing algorithms to treat clouds generally with objective algorithms continues to be an active research topic. While cloud properties derived from existing algorithms can be used where applicable, to achieve our objective, a more general approach is required. We intend to us cloud property retrievals when possible, but not to limit our analysis of cloud radiative feedbacks to the periods when such products are available. What we describe in this section is an approach to this problem that attempts to circumvent the current technological limitations where we use an ad hoc combination of algorithms, parameterizations, and empirical relationships. The scheme is necessarily modular and allows for insertion of additional algorithms as they are developed and shown to be superior to what is currently used. It is important to understand that what we describe below is a first approximation, a baseline, against which new retrieval techniques can be tested and implemented as they are developed.

To derive a generalized cloud property description it is useful to recognize what information we have directly from observations, what cloud properties can be retrieved in a straightforward way from the observations, and what cloud properties can be retrieved from algorithms and which need to be developed from parameterizations. We know the cloud layer bases and tops, the

temperatures of the cloud layers, and the vertically integrated liquid water content (LWP). This information greatly constrains the microphysical and radiative properties of the column. What we don't know is how the LWP should be distributed vertically; we have no direct information on the distribution of ice water either in an integrated or vertically resolved sense; and we have no direct information on particle size.

The critical issue that must be addressed is related to the use of the radar reflectivity and Doppler velocity as quantities that contain information about condensed water and particle size. In nonprecipitating liquid or ice phase volumes where the particles are small with respect to the 8mm wavelength of the MMCR, the radar reflectivity provides information on the square of the water content (Frisch et al., 1998) while for volumes that contain large ice crystals perhaps coincident with liquid water, the radar reflectivity, because it is principally derived from the largest particles, provides information primarily on the condensed mass of the ice phase leaving us with very little information about the liquid phase. The empirical relationships we require, therefore, must provide information on the normalized distribution of liquid water in the vertical column so that we can 1) distinguish between that portion of the LWP derived from warm (i.e. temperature greater than freezing) cloud volumes and that portion derived from supercooled cloud volumes and 2) distribute the supercooled LWP vertically. Kiehl et al. (1998) provides such a parameterization that was derived for use in the Community Climate Model from other empirical data. In future implementations, we will develop a database of such relationships segregated by meteorological type derived from ensemble runs of a cloud-resolving model. It is important to realize, however, that while we use the parameterized profile of LWC *only in a*

vertically normalized sense to provide information on how to distribute the measured LWP within the actual cloud layers observed by the MMCR.

In that portion of the profile where temperatures are warmer than freezing and clouds are observed by the MMCR, we distribute the warm fraction of the LWP vertically using the Frisch (1998) parameterization where the normalized square root of the radar reflectivity is used as a vertical weighting function. In the region of the profile where supercooled clouds are observed by the MMCR and are not cirrus layers (see below), we distribute the supercooled fraction of the LWP vertically according to the empirical distribution function of liquid water within the hydrometeor layers observed by the MMCR. In other words, we have a value of the supercooled water path and we have the layer boundaries of the supercooled layers. The parameterization is used simply as a weighting function to distribute that water within the appropriate cloud layers. The particle sizes of the warm liquid phase volumes are then calculated using a simple expression for effective radius derived from aircraft data and analytical considerations by Dong and Mace (2003): $r_{e,liq} = 19.5\exp(0.0384\, dBZ_e)$ where dBZ_e is $10\log_{10} Z_e$. This expression is assumed valid for $r_{e,liq}<10\mu m$ and is strictly valid only for continental clouds. Effective radii that are diagnosed to be greater than $10\mu m$ are assumed to be possibly contaminated by precipitation and the cloud particle effective radii are set to 10.0 μm. For the liquid phase clouds that exist at temperatures colder than freezing, we simply assume that $r_{e,liq}=5\mu m$.

For cloud ice water content (IWC), we face a more difficult challenge since no integral constraint exists for the total column mass. Cirrus clouds, defined as layers dominated by ice microphysical processes in the upper troposphere, are identified based on a thermodynamic and

radar reflectivity-based definition discussed in Mace et al., (2001). We use a hierarchy of algorithms starting with the approach described in Mace et al., 2002 that uses the radar reflectivity and the Doppler velocity (Z-V algorithm) and returns a profile of IWC and particle size. Since Z-V algorithm is not always available, we use results derived the radar and downwelling IR radiance (Z-R algorithm; Mace et al., 1998; Mace et al., 2005) that provides IWP and layer-mean effective size. If neither the Z-V algorithm nor Z-R algorithm results are available, we use the temperature-dependent regression equations provided Liu and Illingworth (2002) for middle latitude cirrus. When Liu and Illingworth is used, the cloud particle size for cirrus is parameterized using the simple pressure dependent effective radii expression described by Kiehl et al. (1998).

Ice phase volumes that cap deeper cloud layers such as nimbostratus or volumes that are assumed to be potentially mixed phase (i.e. thick altostratus, altocumulus, nimbostratus, and cold boundary layer clouds) are a more difficult problem since there has been relatively little observational treatment relating ice mass and radar reflectivity in these clouds. Aside from the thermodynamics, the routine ARM observations in such clouds are essentially limited to the MMCR Doppler moments observations. Ultimately, physical inversion algorithms are needed to treat these cloud types objectively. However, no such algorithms presently exist. Therefore, our goal is to develop a reasonable approximation of the properties of these clouds using available data in lieu of results from physically-based algorithms. Using a multiple linear regression approach we seek a function of the form,

$$IWC = a + bF_1\left(Z_e, V_d\right) + cF_2\left(T\right) \tag{1}$$

where V_d is the Doppler velocity and T is temperature. Our goal is to find functions F_1 and F_2 that approximately make equation 1 linear in the various terms. The Doppler velocity is a reflectivity-weighted quantity, while the fall speed of a particle is determined by the ratio of particle mass to its area (Heymsfield, 1972; Mitchell, 1996). We assume that the particle area can be expressed in terms of a power law (i.e. $A = a_A D^{b_A}$) where D is the maximum dimension of the particle and b_a has values between 1.3 and 1.8 for ice clouds (Mitchell, 1996). This assumption allows us to express the following proportionality: $IWC \propto V_d D^{b_A}$ where D now represents some characteristic size of the particle population. With $Z_e \propto D^{6-b_Z}$ (b_z typically has values between 2 and 2.5 for ice clouds (Mace et al., 2002)), we can express a proportionality: $IWC \propto V_d Z_e^{b_A/(6+b_Z)}$. The forgoing proportionality is the relationship used for $F(Z_e, V_d)$ in the regression relationship. While we expect the *IWC* to be positively related to the temperature (Heymsfield and Platt, 1984), we expect that a more linear relationship would exist between the condensed mass and the temperature dependent equilibrium vapor pressure. So, we set $F(T) = \exp\left[\frac{L}{R_v}\left(\frac{1}{273} - \frac{1}{T}\right)\right]$ where L and R_v are the latent heat of sublimation and the gas constant for water vapor, respectively.

To derive the coefficients, *a*, *b,* and *c*, we use the in situ microphysical dataset that was collected by the University of North Dakota Cessna Citation during the March 2000 IOP. For the present application, we use data collected in middle tropospheric mixed and ice-phase layers on 3/12, 3/13, 3/17, 3/18, and 3/21. The instrument complement on the Citation included the standard Particle Measurement Systems 2DC to characterize a portion of the particle size distribution

from approximately 100 μm to 1000 μm and the Counterflow Virtual Impactor (CVI; Twohy 1997) to directly measure the condensed mass. The counter flow of the CVI during this IOP excluded particles that ranged in diameter from 7 to 9 μm. While this does not exclude all liquid water, since the flights in question were typically well above the freezing level in altitude, we make the assumption that the condensed mass measured by the CVI in these clouds was due only to the ice phase. Using a bimodal functional fit to the 5-second averaged 2DC size spectra to approximate the full particle size distribution (Mace et al., 2002), we calculate the radar reflectivity using the approach outlined in Atlas et al. (1995) and then calculate the Doppler velocity by combining the bimodal functional approximation of the size distribution and the area and mass measurements provided by the 2DC and CVI (Heymsfield et al, 2002). The calculated Z_e and V_d, the CVI IWC and the temperature measured by the Citation are used in a multiple linear regression algorithm to derive the coefficients for equation 1 (see Table 1). Since the particle size spectra from the 2DC are known to have large uncertainties and do not fully resolve the size spectrum that could be encountered in these clouds, we expect significant uncertainty in the calculated radar reflectivity and Doppler velocity. The CVI mass measurements can also have substantial uncertainty (~15%). Therefore, to remove outlying data points, the measurements are compared to a *Z-IWC* relationship published by Heymsfield (1977) in an extensive analysis of midlatitude deep ice-phase clouds where the relationship $IWC = 0.035Z^{0.505}$ was found. We discard any data whose *Z-IWC* combination is more than a factor of 5 outside of this relationship; thus the filter only excludes true outliers. After processing and filtering data from the flights listed above, we are left with approximately 1500 5-second averages of *IWC*, *T*, and calculated Z_e and V_d, . Figure 6 and Table 2 demonstrate that the regression-based algorithm reasonably approximates the observed IWC in terms of Z_e, V_d,

and *T*. The correlation coefficient of the derived IWC compared to the observations is 0.83 with a bias of 0.2 mg m^{-3} (0.3% of the mean of 64 mg m^{-3}) and median error of 33%. Finally, the particle size of the ice-phase in these clouds is parameterized using the Kiehl et al (1998) parameterization.

The diagnosed condensed water for the 3/1-3/3 period is shown in Figure 7. While for continuity we show the diagnosed liquid water in the periods when precipitation was occurring (background shaded light pink), the liquid water content and path at these times are overestimates because the MWR radome was wet and therefore recorded emission form the condensed water on the radome. The cirrus field on 3/1 and 3/2 that passed over the SGP in the southwesterly flow ahead of the low pressure system is estimated to have had IWP ranging up to about 100 gm^{-2} in the thicker portion near 03 UTC. As the deep cloud structure advanced over the SCF associated with the deepening weather system, precipitation began almost immediately. The IWP during the period as derived from the regression parameterization is estimated to be several hundred g m^{-2}, the MWR-derived LWP is not valid, however, due to rain on the MWR radome. The brief period between rain events on 3/2 when cirrus was observed above a lower layer that existed between 2 and 5 km had total water path near 600 gm^{-2} with just 100 gm^{-2} of that amount due to ice with most of the IWP in the mixed phase portion of the lower layer. The behavior of the condensed water algorithm described above is evident in the various features of the cloud field on 3/3. The boundary layer cloud was always warmer than freezing and the high cirrus features were estimated to be all ice. The cloud that passed over the SCF between 17 and 18 UTC between 4 and 5 km was in the temperature range between 274 and 260 K and was deemed to be mixed phase. Note that the microwave radiometer retrieval of LWP shows a definite increase

between 17 and 18 UTC that does not appear to correspond to an increase in the radar reflectivity of the stratocumulus in the boundary layer.

Radiative Properties and Radiative Fluxes

With the microphysical properties of the profiles estimated, published parameterizations are used to estimate the radiative properties of the cloudy volumes. These parameterizations depend typically on the condensed water content and some measure of effective particle size. For the shortwave radiative properties of condensed liquid, the parameterization described by Slingo (1989) is used, and the simple radiative parameterization described by Kiehl et al. (1998) is used for the longwave radiative properties of the liquid phase. For the ice phase, we use the Fu (1996) and Fu et al. (1998) parameterizations for the shortwave and longwave radiative properties, respectively. The cloud radiative properties are then combined with the radiative properties of the clear atmosphere to calculate the profiles of solar and longwave radiative flux. The radiative transfer model uses a two-stream approximation given by Liou (1974) and the solution algorithm is developed by Toon et al. (1989). The k-distribution method described by Kato et al.(1999) with the correlated-k assumption provides estimates of the gaseous absorption optical thickness of water vapor, ozone, carbon dioxide, and oxygen in the shortwave spectral region using 32 spectral intervals between 0.25 and 4.5 μm. In the longwave, the radiative properties of the gaseous constituents (including O_3, H_2O, N_2O, and CH_4) are derived using the approach described by Mlawer et al. (1997) and the two-stream longwave fluxes are derived using 16 bands between 3.2 and 52μm.

Figure 8 shows two specific examples of the CPC results during the 3/1-3/3 period. The heating rates that we show here are instantaneous values calculated from the 5-minute averaged profiles expressed relative to the clear sky. In other words, we have subtracted the instantaneous clear sky heating rate from that diagnosed in the cloudy sky to show the cloud induced heating. At 2245 UTC on 3/1, a pulse of cirrus was passing over the SCF in the southwesterly flow ahead of the advancing storm system. The layer at this time extended from 7.5 to 9.5 km and, using the retrieval algorithm described by Mace et al., (2002), the IWP of the layer was estimated to be 18 g m^{-2} with the IWC peaking in the middle of the layer. With an effective radius of 28 μm, the layer optical depth was estimated to be approximately 1.6 at this time. We diagnose weak solar heating in this layer that peaks near the middle of the layer at approximately 1 k day^{-1}. In the IR, we find cloud base heating of approximately 5 k day^{-1} changing to cloud top cooling on the order of 4 k day^{-1}. We discuss validation of the microphysical and radiative quantities below and the uncertainty of the derived heating rates in Part II.

At 1700 UTC on 3/3, three cloud layers were observed by the MMCR. During this period, the lower stratocumulus layer was thinning with occasional breaks in the layer passing over the SCF. Above the boundary layer clouds at this time, a 2 km deep layer based near the freezing level passed overhead while cirrus, barely sensed by the MMCR, was observed in the upper troposphere. The total liquid water path at this time was retrieved from the MWR (Figure 3) and reported to be 60 g m^{-2}. Since both the boundary layer cloud and the middle level layer could have potentially have had liquid water, the parameterization discussed earlier is used to distribute that water among these layers. The lower layer is attributed the majority of the water (45 g m^{-2}) with the remainder assigned to the super cooled portion of the cloudy column. Because the

determination of the liquid and ice water contents of layers in the mixed-phase temperature region are independent of one another, we find in this layer that the ice water path (100 g m^{-2}) derived from equation 1 is substantially larger than the liquid water path of this layer. Note the visible extinction profiles of the liquid and ice phases of this layer are nearly identical resulting in an optical depth of 12. The cirrus near 8 km is diagnosed to be quite tenuous with a water path from the Liu and Illingworth (2002) regression of approximately 0.5 g m^{-2} and optical depth near 0.1. The heating profile in this column is dominated by strong cloud top cooling of the mid level layer compensated somewhat by weak solar heating. Interestingly the cloud top of the boundary layer cloud does not cool substantially due to the presence of the optically thick layer above it although there does appear to be weak cloud base warming of the boundary layer cloud. Perhaps it is the presence of the mid level clouds that resulted in the thinning and partial dissipation of the stratocumulus through suppression of radiative destabilization of the cloudy boundary layer.

In Figure 9, we show the cloud induced radiative heating for the storm system that passed over the SCF between 3/1 and 3/3. The largest convergence of radiative flux occurred near the cloud top region of the mixed phase and low clouds in the middle lower troposphere. Solar heating in the optically thick portions of this region averaged 2-3 k day^{-1} while some solar cooling is noted in the surface layer below the mean cloud base where the thicker clouds above attenuated solar radiation that would have been absorbed by water vapor in the boundary layer. The upper troposphere experienced primarily heating in both the solar and IR associated with the cirrus that occurred in advance of the storm system on 3/1. The time-averaged net heating profile for the 72 hour period shows cloud-induced cooling in the lower troposphere and heating aloft for a net

atmospheric radiative effect of -7 W m^{-2} due primarily to the a net loss of IR energy. Overall the surface experienced 9 W m^{-2} of heating during this period (+14 W m^{-2} in the IR and -4 W m^{-2} in the solar) and the TOA experienced +3 W m^{-2} of heating (-5 W m^{-2} solar and +8 W m^{-2} in the IR). For completeness, we include error bars with these quantities derived using the validation statistics presented below and the technique outlined in Part II. Obviously, the uncertainties in the derived radiative effects are significant.

2.3 Validation of the Column Physical Characterization

Our approach to characterizing the physical state of the atmospheric column using ground-based remote sensing data is unique since we merge many data sources through an ad hoc combination of parameterizations and retrievals linked together through various assumptions. Random and systematic error can enter the process at any point and this error has the potential to become amplified through the processing algorithms we employ. Therefore, it is critical that the results are validated carefully with independent observations. Clearly, the most appropriate validation of this approach would come about by comparing the cloud microphysical properties with in situ aircraft data. This has been accomplished for the algorithms we apply to boundary layer clouds (Dong and Mace, 2003; Dong et al., 2003) and cirrus clouds (Mace et al., 1998, Mace et al., 2001, Mace et al., 2002; Mace et al, 2004). An independent aircraft dataset to test the mixed phase retrievals requires in situ measurements of ice water content and particle size distributions in conjunction with ground-based Doppler radar and MWR observations. To our knowledge, an additional dataset like that collected in 3/2000 over the SGP does not exist although we do show a comparison of the ice phase regression parameterization in Figure 6 and Table 2. In lieu of

more detailed in situ comparisons, we use comparisons with radiometric quantities measured and retrieved at the ground and the TOA. Since the derived radiative properties of the clouds and their calculated effects on the radiation streams would accumulate errors, any significant problems with our analysis technique would become apparent in systematic biases and RMS differences compared to observations. We use retrievals of the cloud optical depth from multi filter rotating shadowband radiometers (MFRSR) as well as flux observations at the surface and the TOA for validation with the assumption that reasonably unbiased comparisons of the CPC results with these quantities is sufficient to establish the skill of the technique for the stated purpose of evaluating the radiative feedbacks of clouds.

The cloud optical depth record that we use for validation is derived using the algorithm described by Min and Harrison (1996a) and Min et al. (2004a). Min and Harrison (1996a) developed a family of inversion methods to infer optical properties of clouds from diffuse measurements at the multi-filter rotating shadowband radiometer (MFRSR) 415-nm channel, together with cloud liquid water path from MWR. The MFRSR allows accurate determination of atmospheric transmittances at 415, 500,615, 673, 870, and 940 nm without requiring absolute calibration because it measures both total horizontal irradiance and direct-normal irradiance using the same detectors by a blocking technique. Consequently Langley regression of the direct-normal irradiance taken on stable clear days can be used to extrapolate the instrument's response to the top of atmosphere, and this calibration can then be applied to the total horizontal irradiance during overcast periods. Transmittances are calculated subsequently under cloudy conditions as the ratio of the uncalibrated MFRSR signal to the extrapolated top-of-atmosphere value. The cloud optical depth and cloud drop effective radius are simultaneously retrieved through the use

of a nonlinear least squares minimization in conjunction with an adjoint method of radiative transfer (Min and Harrison, 1996b). Min at el. (2004a) take advantage of simultaneous spectral measurements of direct and diffuse transmittance of an MFRSR and temporal variations to retrieve optical depths for optically thin clouds from direct beam irradiances. To minimize the interference of gaseous absorption, the retrieval algorithm selects the 415 and 860-nm channels, and separates aerosols from thin clouds based on their temporal and spectral characteristics. The thin cloud algorithm provides accurate retrievals of optical depth for clouds with visible optical depth < 5. Various comparisons and validations for the narrow band retrieval algorithm of Min and Harrison (1996a) have been reported (Min and Harrison, 1998; Barnard et al, 2001; Min et al., 2003). An uncertainty analysis of thin cloud retrievals has been conducted and shows that it produces retrievals that are better than 5% or 0.05 when cloud optical depth is less than 1 (Min et al. 2004a).

The optical depth comparison for the case study period is shown in Figure 10 (note that no MFRSR observations are available on 3/2). For optical depths less than 5, we are especially sensitive to horizontal variations in cloud structure due to the use of direct solar beam transmittance in the MFRSR optical depth retrieval. While the overall comparison on this day is reasonable, the trend observed by the radar retrievals is not identical to the MFRSR retrievals during the middle portion of the day when, according to Figure 5, the cirrus layer thinned considerably in the vertical column directly above the radar. However, the overall comparison of the instantaneous optical depth values of this cirrus event appears reasonable. On 3/3, the clouds observed at SGP, range from optically and physically thin stratocumulus to optically thick multilevel clouds (Figure 5). The CPC and the MFRSR retrievals (Figure 11) capture this

variability in the optical depth time series with remarkable agreement. We find the optical depth varying between 10 and approximately 200 on this day and the optical depths derived from the two independent techniques track one another with precision. In order to perform a more rigorous comparison, we examine the months from February through December 2000. To minimize sensitivity to horizontal variations in cloudiness that might influence the hemispheric spectral flux measurements we average the CPC and MFRSR observations for 30 minutes and exclude any periods with less than 80% cloud occurrence as derived from the MMCR data averaged over this 30-minute interval. In the optical depth range less than 5, we also restrict the time period to the hours surrounding local solar noon (17-21 UTC). Recall also, that the CPC is not reliable during precipitation and therefore these periods are excluded. The comparison shown in Figure 11 is summarized in Table 3. Overall we find a high degree of correlation and a 50% positive bias (CPC higher) over a four order of magnitude range in optical depth. The apparent negative bias in the optically thin clouds is at least partially due to aerosol that is not included in the CPC. The high optical depth events include warm liquid phase layers like on 3/3 but also deep and mixed phase cloud layers where the cloud microphysical properties are derived with the mixed phase cloud parameterization scheme. The optical depth comparison is encouraging because it lends some degree of credence to our characterization of the cloud microphysical properties although the positive bias needs to be kept in mind.

In order to examine the radiative heating of the atmosphere due to clouds, we must also consider to what degree of precision the solar and IR radiative fluxes at the surface and TOA can be characterized. The TOA flux values are not direct measurements but are derived from half-hourly GOES-8 data using a set of narrow- to broadband conversion algorithms. These

algorithms are of the same form and derived in the same manner as those reported by Minnis and Smith (1998). However, they are based on correlations between 1998 GOES-8 visible (0.65 μm) and infrared (10.8 μm) radiances and their respective shortwave (SW; 0.2-5 μm) and longwave (LW; 5 – 100 μm) flux counterparts from the Clouds and Earth's Radiant Energy System (CERES) scanner (Wielicki et al., 1998) on the Tropical Rainfall Measuring Mission (TRMM) satellite. The RMS errors in SW albedo and outgoing LW radiation (OLR) regression fits to the TRMM data are 0.021 and 7.2 Wm^{-2}, respectively, or 8.3 and 2.8%. The regression formulae were applied to the 2000 GOES-8 data calibrated using the TRMM Visible Infrared Scanner as in Minnis et al. (2002).

Additionally, the GOES data are used to derive cloud amount, altitude, temperature, and visible optical depth using the Layer Bispectral Threshold Method (LBTM), which was applied to hourly GOES-8 data taken between 1995 and 2003 over a 10° latitude by 14° longitude domain centered on the SCF (Minnis et al. 1995; Khaiyer et al., 2002). The LBTM uses the RUC temperature and humidity profiles to account for atmospheric attenuation of the visible and infrared radiances and a set of fixed ice and water cloud models to derive optical depth from the reflected radiance fields (Minnis et al. 1993). Both the cloud properties and TOA fluxes are averages for a 0.3° region centered on the SCF.

At the surface, ARM deploys a suite of well-calibrated up and down looking solar and IR broadband radiometers, and these data streams are used here, averaged to the 5-minute time resolution of the CPC, for comparison. In an effort to effectively characterize the effects of clouds on the solar flux, we combine the observed downwelling solar flux with estimates of the

clear sky solar flux derived using the procedure described in Long and Ackerman (2000). Use of this quantity allows us to estimate the effects of clouds on the solar flux and to examine the fractional change in downwelling solar flux due to clouds. Similar quantities can then be calculated from the CPC diagnostic using the cloudy sky and clear sky solar flux calculations. Since no similar estimate of the downwelling clear sky IR flux has been devised, we examine just the cloudy sky downwelling and net surface longwave flux instead of the surface longwave cloud effect.

When performing the radiation calculations we assume that each column is independent and plane parallel and that the observed vertical distributions of clouds during the 5-minute averaging period correspond to layers that are overcast. As an example, we complete our description of the 3/1-3/3 case study by comparing the calculated fluxes to observed TOA and surface fluxes in Figure 12. The time series comparisons suggest reasonable agreement in all quantities with some notable exceptions. On 3/1, the cirrus increase the TOA albedo from approximately 20% to as high as 45% late in the day when the layer thickened and the zenith angles increased. The calculations track the GOES-derived albedos quite well while at the surface the variability in the downwelling solar also suggests reasonable agreement. A notable bias is discernable in the surface solar downwelling fluxes. This is due, at least partially, to the fact that our calculations do not include aerosol – an omission that would cause only small biases when considering the cloud-induced radiative perturbations. The OLR values on 3/1 shows significant offsets during much of the day and only come into agreement after about 21 UTC when the clouds thicken. At the surface, a persistent 5-10 Wm^{-2} bias seen between the thick cloud events may be due to thicker clouds that are not observed by the vertically pointing

MMCR at that time. However, the peaks in emission that correspond to the periods when the thicker portions of cirrus are overhead show good agreement. During the remainder of the period, we find that the albedo agrees well although the variability observed by the satellite is much less than derived instantaneously from the surface data. This difference in variability is due to the smoothing effect of averaging over a larger area in the GOES data. The OLR continues to show occasional biases particularly on 3/3 suggesting perhaps that thin cirrus that was not observed by the MMCR resulted in a 10-15 W m^{-2} high bias in the calculations. Overall, the surface solar flux agrees very well in the heavy overcast periods while the downwelling IR shows a persistent 5 W m^{-2} bias through 3/2 and 3/3 for which we have not been able to determine a cause. With respect to the profiles we considered in Figure 8, Table 4 summarizes the flux comparisons.

While case studies are useful, a long-term comparison of fluxes allows for a more rigorous characterization of the CPC errors. The objective of this initial study is not to consider partly cloudy skies or periods where the cloud properties are rapidly changing. While we recognize the importance of such situations, it is more instructive to minimze this source of variability so that the validity of the cloud properties can be discerned. Therefore, we consider only situations that meet specific criteria during 30-minute averaging periods centered on the GOES observation times. We define the vertical cloud occurrence fraction during this period as the fraction of original 36-second MMCR columns that have cloudiness reported at some level. Since the GOES algorithm also estimates a pixel level cloud amount, cloud base, and cloud top, we additionally require the satellite pixel(s) nearest the SCF to have a similar cloud cover and to be of a similar type. For the purpose of this comparison, middle level clouds are defined to have

bases greater than 3000 m and tops less that 6500 m. High clouds are defined as layer with bases above 6500 m while low clouds have tops below 3000 m. We define clear as a cloud occurrence fraction of 0 during a particular time period while broken clouds are assumed to have an occurrence fraction greater than 0.5 but less than 0.9. A period with scattered cloud cover has occurrence fraction greater than zero but less than or equal to 0.5 while overcast has occurrence fraction greater than or equal to 0.9. For comparison of the TOA and surface in a 30-minute period, we require the cloud coverage to be of the same class (scattered, broken, or overcast). Also, the cloud type of the highest layer observed by the MMCR must be the same as the highest cloud type derived from the GOES data. With these constraints and definitions, we are able to reasonably evaluate the CPC, although, in order to acquire sufficient data to make the comparisons, we are forced to examine a long time period.

Using data collected at the SCF during the year 2000, we compare several key quantities in figure 13 for overcast cloud scenes and summarize the comparisons along with broken cloud scenes in Table 4 where we show several quantities. At the TOA we include the upwelling IR flux ($L\uparrow_t$; W m^{-2}), the upwelling solar flux ($S\uparrow_t$; W m^{-2}), and the solar cloud effect ($CFC - NS_t$; W m^{-2}) defined as the difference in the net solar flux in cloudy skies from the net solar flux in clear skies where downward fluxes are considered positive. At the surface we show the downwelling IR flux ($L\downarrow_s$; W m^{-2}) and the surface solar cloud effect ($CFC - NS_s$). Since we are not attempting to model the effects of aerosol on the solar flux, at the surface we compare the fraction of the downwelling clear sky flux that has been removed by cloud ($S\_Frac\downarrow_s$) where the clear sky surface solar flux observations are derived from the technique described by Long and Ackerman (2000). At the TOA, the $CFC - NS_t$ observations use clear sky values

derived from nearby pixels deemed to be clear. We do not attempt to show longwave cloud effect ($CFC - NL$) at either the surface or TOA. At the surface no clear sky equivalent derivations of upwelling or downwelling longwave fluxes are available, and at the TOA, the clear sky flux derived from nearby clear scenes will have a very different surface temperature and perhaps a different moisture profile than what is observed at the SCF. It is therefore, impossible to compare the calculated longwave cloud effects with the observations.

Overall, the comparisons shown in Figure 13 and Table 5 are reasonable although we find significant scatter and some biases in several of the quantities. The solar radiation fluxes at the surface and TOA are, of course, very sensitive to the horizontal structure of the cloud field and the representativness of the 30-minute averaged CPC vertical profiles. It is encouraging to note that $S\_Frac\downarrow_s$ is essentially unbiased and that the scatter as measured by the median error and the normal deviation both decrease significantly in overcast scenes compared to broken scenes. These statistics are similar to those presented in a radiation closure study (Mace et al., 2001) using cirrus cloud retrievals. The negative bias in $CFC - NS_t$ that is very evident in Figure 13a is expected because the upwelling flux observed by GOES in nearby cloud-free pixels includes an aerosol contribution that would tend to reduce the observed cloud effect relative to an aerosol-free calculation. The bias evident in Figure 12c in $CFC - NS_s$ amounts to about -9% according to Table 5. While we are using a consistent representation of the surface albedo as derived from the ratio of the observed cloudy sky broadband values in the clear and cloudy calculations as well as in the estimate of the clear sky upwelling value, it is unclear at the present time the degree to which aerosol might modify the observed cloud effect relative to a no-aerosol calculation although it is encouraging that $S\_Frac\downarrow_s$ is unbiased.

Compared to the exhaustive validation presented by Rossow and Zhang (1995), our results suggest validity at least comparable to their ground-based comparisons although, as expected, we have significantly more scatter in our TOA comparisons. This is not surprising, however, given the technique used in satellite retrieval studies where derived irradiances (ERBE) are used to validate a product derived from a set of narrow band radiances and reflectances where the clouds serve essentially as a transfer function to convert between the narrowband measurement and the broadband fluxes (Rossow and Zhang, 1995). Highly correlated unbiased comparisons would be expected in such circumstances. In our case, we do not use radiances or irradiances in the retrievals and, therefore, validation with radiation measurements at the surface and TOA is reasonable and instructive. Based on our comparisons with MFRSR optical depths where nearly unbiased agreement was found relative to the factor of 1000 variation in the quantity, and based on small biases in the TOA and surface flux quantities, we conclude that the CPC technique applied to ARM data can reasonably characterize the macroscale properties of clouds as well as the gross effects that the clouds impose on the solar and infrared radiation streams. The quantitative uncertainty in the cloud radiative effect and cloud radiative forcing is discussed in detail in Part II.

3. ISCCP and LBTM Comparison

The climatology's of CTP and τ_{tot} such as those produced by ISCCP and by ARM using the LBTM (Minnis et al. 1995, Khaiyer et al. 2002) are becoming standards against which many models are being evaluated. Zhang et al. (2004), for instance, found that of the 10 GCMs they

examined, all significantly underpredicted the global occurrence of middle level clouds and significantly overestimated optical thickness relative to the satellite-derived results. Because such conclusions have far-reaching implications for model development and interpretation, we compare the CTP and total column optical depths (τ_{tot}) derived from the ARM data analysis to similar quantities derived from the ISCCP (Rossow and Schiffer, 1991, 1999) and by the LBTM algorithm. Both satellite algorithms use visible and thermal infrared measurements from available weather satellites, combined with meteorological analyses, to derive physical descriptions of the atmospheric column very much like we are creating with ground based data from the SCFs except that the satellite results are global and extend over many years (decades in the case of ISCCP). While RZ95 and others have evaluated ISCCP using TOA and some ground-based radiation measurements with reasonable results, a statistical comparison of the satellite results with long-term ground-based measurements of cloud top pressure and derived optical depth has not been reported.

The ISCCP algorithm samples the geostationary pixel-scale satellite data in 3-hourly intervals and at 30 km horizontal spacing. Therefore to build up reasonable statistics for the comparison of ISCCP to ARM data, we derive the mean and standard deviation of the ISCCP values in 100 km and 250 km domains that are centered on the ARM SCF. The LBTM retrievals are calculated and recorded for every available image at the pixel scale. We have examined statistics from the pixel nearest the ARM SCF and statistics derived from the 8 surrounding 0.3° regions with similar results. Figure 14 shows the frequency of occurrence histograms of joint CTP and τ_{tot} for March 2000 as reported by ISCCP, LBTM, and derived from the ARM data along with results from an algorithm that has been developed (ICARUS; Webb et al, 2001) to take predicted, or in

our case diagnosed, cloud property profiles and convert them into radiance and reflectance that would be observed by the satellite radiometers and then mimic the ISCCP CTP quantity. A major part of the ICARUS algorithm as applied to model output is to account for the spatial cloud fraction and overlap. Here, since we are dealing with point measurements, we only derive the ISCCP-estimated CTP with the ICARUS algorithm.

In Figure 14, both similarities and differences can be seen. The two satellite algorithms appear similar in the upper troposphere except that ISCCP places much of the optically thin cirrus into the upper left bin. Both algorithms show a minimum of occurrence in high clouds of medium optical thickness. Both satellite algorithms also diagnose maxima in middle and lower tropospheric optically thick clouds and find deep optically thick clouds near 400 mb. LBTM diagnoses more lower tropospheric optically thin clouds than does ISCCP. The ARM data show similar peaks in occurrence of optically thick lower tropospheric clouds although the optical depths are somewhat higher and more optically thick low clouds are found. In the upper troposphere, thin cirrus predominates and more clouds of medium optical thickness are found compared to the satellite algorithm results. The most obvious differences exist in the lower and middle tropospheric clouds of medium optical thickness which the ISCCP and LBTM find more frequently than either ARM or the ICARUS simulation. The ICARUS results do tend to increase the frequencies in this region although not to the extent diagnosed by the ISCCP or LBTM algorithms.

To better understand the differences in the histograms, it is instructive to compare the actual timeseries of CTP and τ_{tot}. For reference, we show the diagnosed condensed water height time

section for March 2000 in figure 15a. The CTP and τ_{tot} timeseries are in Figures 15b and 15c where we plot the hourly averaged quantities derived from the ARM data for clarity; the 5-minute data show more variability that obscures important details. From a broad perspective, the comparison is encouraging with ISCCP and LBTM reasonably capturing the variability in the evolving cloud structures over the SGP region during this month as compared to the ARM diagnostics. A closer examination reveals the sources of the differences noted in Figure 14.

Between the two satellite algorithms we find that the primary source of the differences in Figure 14 is from the CTP quantity. The optical depths derived by ISCCP and LBTM are very similar through the month. With respect to CTP, thin cirrus events show the largest discrepancies between the satellite algorithms and observations. ISCCP has a tendency to place these optically thin clouds into a default pressure bin at 100 mb while LBTM often diagnoses these clouds in the middle and lower troposphere (i.e. 3/2, 3/9, 3/28). The best example of this is on 3/1 when LBTM places much of the thin cirrus between 700 and 800 mb. Other discrepancies are evident such as on the 3/18 when ISCCP places the thick mid and low level overcast cloud well into the boundary layer while LBTM reports clouds more in the middle troposphere above the measured cloud tops. With the exception of thin cirrus in ISCCP, we find that the satellite algorithms nearly always bias CTP lower than the measurements when they are biased. This seems to occur especially in multi layer situations when cirrus occur above thick mid and low level clouds (i.e. 3/3, 3/7, 3/16) and occasionally in thick cirrus/altostratus (i.e. 3/13). When thin cirrus are present over mid- and low-level clouds, the satellite algorithms place clouds somewhere between these two cloud layers. Curiously, this bias into the middle troposphere also occurs in low clouds on 3/30 although there may have been higher clouds in the area not yet over the SCF.

With the exception of the possibility of being biased low due to tenuous cloud tops and attenuation in thick clouds, the CTP from the ARM data is an observation while the satellite-derived CTP is more of a derived quantity; especially in clouds with τ_{tot} less than about 5 where the clouds are partially transmissive and the radiating center of the cloud is not at the cloud top.

For τ_{tot} we find that the ARM CPC diagnostic correlates well with ISCCP and LBTM. We find reasonable agreement in the optically thinner cirrus clouds such as on 3/1, 3/6, 3/9, 3/21, and 3/31. Clouds of medium optical thickness also show reasonable agreement such as on 3/10, and 3/13. When ISCCP and LBTM disagree with the ARM diagnostic in the thin and medium optically thick clouds the optical depth bias tends to be low. An example of this is on 3/2 and 3/3 which we examined earlier in the case study analysis. Overall, the satellite algorithms are 30-50% lower than the values diagnosed with the ARM data on these days. The ARM τ_{tot} is generally higher than the satellite algorithms in very thick clouds like those that persisted from 3/15-3/19. The ISCCP and LBTM use reflectance models that maximize at optical depths of 256 and 128, respectively, because of the reflectance field changes very slowly with increasing optical depths above 128. The difference in the reflectance for clouds with optical depths of 128 and 256 is within the uncertainty of most satellite visible channel calibrations. We note that only rarely is the ISCCP τ_{tot} greater than the ARM τ_{tot} such as on 3/22 and 3/23.

Given just three observations per day for ISCCP and only daylight data from LBTM, a single month is not sufficient for quantitative comparison. We attempt a more rigorous comparison of CTP and τ_{tot} by examining data from the year 2000 and apply the criteria used in the radiative closure study of the previous section where only overcast uniform cloud conditions are

considered. Figure 16 shows several selected scatter plots and Table 6 summarizes the overall comparison of the various comparisons. Several general results can be seen. The ICARUS simulation of the ISCCP retrieval improves the CTP comparison to the ARM data. Even though the ICARUS result is strictly only defined for the ISCCP retrieval, we also compare it with the LBTM retrievals with similarly improved results. Table 6 shows that the correlation, the linear regression, and the normal deviation tend to improve. The only apparent drawback is the tendency to induce a slight negative bias in the LBTM results. For τ_{tot} the situation is less favorable. A clear negative offset seems to exist in the comparison of the satellite algorithm results compared to the CPC diagnosed values with a bias on the order of 4 db. Agreement tends to be best in the optical depth 1-10 range with significant scatter at lower optical depths and a large negative offset of the LBTM and ISCCP values at the higher optical depths.

4. Summary and Conclusions

We use continuous ground-based data collected at the ARM SCF to characterize the physical properties of the atmospheric columns including cloud occurrence, microphysical and radiative properties, and radiative fluxes. Objective algorithms presently exist to derive the microphysical properties of certain classes of clouds from millimeter radar data combined with other data sources. Several of those algorithms are employed in this work. There are, however, significant gaps in our ability to objectively retrieve cloud properties in the presence of deep and mixed phased clouds. The essential difficulties reduce to identifying what fraction of the liquid water path in such situations is due to clouds that exist at temperatures above freezing and what fraction of the total water path exists at supercooled temperatures. Beyond this, algorithms for

identifying the condensed water contents, both ice and liquid, in supercooled clouds are presently not well established. Therefore, we employ a simple parameterization of condensed liquid water content (Kiehl et al., 1998) that produces a normalized distribution function with which we estimate the fraction of the observed liquid water path that is warm and supercooled. To the warm cloud layers, we apply published cloud property retrieval algorithms and to the cold liquid component, we use the distribution function derived from the Kiehl et al parameterization combined with the MMCR observed clouds and the supercooled LWP to parameterize a liquid water content profile. The IWC in mixed phase clouds is estimated from a new empirical relationship that is derived from a unique aircraft data set that includes measurements of both the particle size distribution and the IWC. Particle sizes are retrieved where possible and parameterized where retrieval algorithms are not applicable. To this microphysical description, standard radiative parameterizations are applied and the upwelling and downwelling solar and IR fluxes are calculated. Since we assume that the radar reflectivity contains condensed water content information, the algorithm is not applicable when precipitation contaminates the vertical profile. The occurrence of precipitation is diagnosed from the MWR brightness temperatures using an empirical algorithm described in the Appendix and by the occurrence of a radar bright band in the MMCR profile of radar reflectivity.

Validation of this scheme comes from various sources. We establish validity and uncertainty based on flux closure at the surface and TOA. Summarized in Table 5, we find for the year 2000 in uniform overcast skies, that the calculations are strongly correlated to measurements with biases in the flux quantities at the surface and TOA of less than 10% and median fractional errors ranging from 20% to as low as 2%. We also compare our derived optical depths with optical

depths derived from an independent technique using MFRSR that has itself been extensively validated (Min and Harrison, 2001). In the optical depth comparison for uniform overcast skies during the year 2000 (summarized in Table 3) we find, a mean bias of 46% with a median bias of less than 10% and a 0.89 correlation coefficient. The slope of the linear regression line is 0.86 with a normal deviation of 20% about this line. Most importantly, the high optical depth cases where the mixed phase parameterization is employed shows very good agreement with the MFRSR retrievals allowing us to have some confidence in the results of the column physical characterization (CPC) technique.

As an initial application, we compared the results of the CPC with retrievals of cloud top pressure (CTP) and total column optical depth (τ_{tot}) produced by two satellite algorithms, ISCCP and LBTM. These satellite products are presently being used for evaluation of climate models. While the satellite products are correlated with the ground-based measurements, we find a decided tendency for the CTP to be biased into the middle troposphere for optically thin clouds and for the optical depths derived from the satellite algorithms to be underestimated. The tendency for the middle tropospheric CTP bias is largely mitigated by application of a satellite simulator algorithm (ICARUS; Webb et al., 2001). As for the findings of Zhang et al. (2004) who found that GCMs generally are producing too little middle level cloud and are biased high with respect to optical depth, our comparison supports the former conclusions but suggests that the latter finding may be premature given the optical depth comparison in Figure 16 and Table 6 where τ_{tot} from the satellite algorithms tends to be significantly low in clouds of high optical depth. It is possible that the tendency for the solar reflectance to asymptote as the optical depth increases, limits the precision of the satellite algorithms at high optical depth (greater than about

60-70). It seems clear that this issue should be examined more carefully before GCM parameterizations are adjusted with the intention of making the predicted optical depths come into agreement with ISCCP and LBTM.

In addition to the satellite algorithm comparison, our findings from this work suggest that ground-based remote sensors can, with reasonable and quantifiable precision, characterize the physical properties of the atmospheric column when using some combination of existing algorithms and parameterizations. In a companion paper (Part II) we show that heating within the atmosphere due to deposition of radiative flux in clouds can also be examined using long-term ground-based data. Given the simplicity of the diagnostic technique we apply to the ARM data, these results establish a baseline against which other more sophisticated algorithms can be compared; i.e. a metric. An algorithm designed to improve the characterization of microphysics so that the radiative properties of the column are more accurately or precisely estimated should be able to demonstrate measurable improvement in the boundary flux comparisons or in the total optical depth comparison shown here.

Since the approach we have taken can be improved upon substantially with the use of more sophisticated cloud property retrieval algorithms, the fact that such simple schemes are able to describe the essential characteristics of the cloudy atmospheric column deserves comment. The ARM observations provide the basic quantities that constrain the atmospheric physical state, namely the vertical location of clouds and the total condensed liquid water. Along with the vertical distribution of Doppler radar observations in the ice phase parts of deep clouds, the observations seem to constrain the problem, even with the use of climatological or parameterized

estimates of cloud particle size in the mixed phase clouds. One could argue that, to first order, the cloud location and total column water are what must be predicted by a GCM in order capture the essence of the radiative feedbacks by clouds and that the precise details of the cloud microphysics may be of secondary importance, at least relative to the present skill of climate models to predict cloud feedbacks (Zhang et al., 2004).

Appendix.

The preliminary data reduction that we conduct to enable the diagnostic analysis described in section 2 is an important component of our overall analysis procedure. In the following paragraphs, we describe the instruments, datastreams, and methodologies that we have developed for this purpose.

Microwave Radiometer

The Microwave Radiometer (MWR) measures downwelling microwave radiation emitted from the sky at 23.8 GHz and 31.4 GHz from which the column integrated liquid and water vapor burdens are estimated. Liljegren et al. (2001) describes the features of the MWR used at the ARM sites and the data inversion algorithms that convert the microwave signals into condensed and vapor column amounts.

One of the key issues in using the MWR in our diagnostic study is the need to avoid periods when precipitation is occurring or when the window in front of the microwave reflector is wet due to dew or precipitation that is ongoing or has recently ended. When the radome is wet, the MWR radiance measurements are biased by emission from the water on the radome (there is also an increase in MMCR noise due to emission by standing water on the MMCR radome). The period of radome drying after wetting by rain or dew is the most difficult problem since the timescale for drying depends on many variables including sunlight, wind, ambient humidity, and

the degree of wetness of the radome. Therefore, we have developed an empirical approach to identify wet radome events based on the observed brightness temperature, outside air temperature, and sky imagery. Invoking the Rayleigh-Jeans law, we assume the brightness temperature measured by the MWR is linear with the emitting temperature of the water on the radome (taken as the outside air temperature), and a simple empirical formula is developed that predicts a threshold brightness temperature above which a wet radome could be expected. This threshold temperature was estimated by examining Total Sky Imager (TSI) images that document the presence of water on the silvered dome before and after cold and warm rain and noting the threshold brightness temperatures recorded by the MWR and the ambient outside air temperatures recorded by the Surface Meteorological Observing System (SMOS). A simple linear equation was then derived that predicts a threshold 31 GHz brightness temperature above which it is likely that the MWR radiance is contaminated by condensed water on the instrument. Our goal is simply to avoid wet radome periods in our long-term processing of ARM data and therefore we choose a reasonably conservative threshold. Figure 3 shows the time series of MWR brightness temperature, and retrieved liquid and vapor with the periods we estimate as wet during the 3-day case study period.

Thermodynamic Profiles

Since we seek to describe the state of the atmosphere at the SCF on a continuous basis over long periods of time, it is necessary to have an accurate and reasonably continuous description of the atmospheric thermodynamic state. Continuous thermodynamic profiles are required to help identify certain cloud types and to perform radiative transfer calculations. To accomplish this,

we combine several sources of information regarding the thermodynamic state to generate what we have termed the merged sounding product. The thermodynamics profiles are ultimately defined on a 90 meter height and 1 minute time grid and consist of temperature, pressure, and water vapor mixing ratio. A 1-minute time step was chosen due to the existence of 1-minute averaged microwave radiometer retrievals of water vapor path.

Sources of information for the merged sounding include radiosondes launched at the SCF, surface meteorological measurements from the ARM facility, MWR-derived precipitable water vapor, radiosondes launched from the Norman, Oklahoma National Weather Service (NWS) site, and mesoscale model output. Optimally, we prefer a continuously observed set of data of sufficient temporal and spatial detail to capture the evolution of the thermodynamic fields. This requires typically at least three hourly radiosonde profiles. Due to budgetary constraints, radiosondes have been launched on a somewhat irregular schedule at the SCF over the history of the ARM project. For example, during the middle and late 1990's, 3-5 soundings per day were launched from the SCF during regular daytime working hours Monday-Friday. No soundings were launched from the end of the workday on Friday until the first sounding early Monday morning. To maintain a continuous record, therefore, we augment the ARM soundings with the Norman NWS soundings (launched twice each day at 2330 and 1130 UTC), and, when the Norman soundings are not available, with the operational NCEP mesoscale model output from either the ETA or RUC models.

The methodology we use for processing the radiosonde and model output data into a continuous time series is described by Mace et al. (1995). Briefly, we begin with the radiosonde data files

available in the ARM archive or the NWS files. These files generally contain several hundred to several thousand data points more or less equally spaced between the surface and the altitude where the balloon bursts. These data points are collected in the vertical bins where additional quality control is applied. The observations in each bin are then averaged. Account is also kept of the time of the observations in each vertical bin. A time grid is then defined (1 minute) and the vertically averaged sounding data are linearly interpolated to it. When more than four hours exist between data points in any height bin, the profile is flagged as missing. Missing profiles are then filled by available Norman NWS soundings, RUC or ETA model soundings. Finally, since surface meteorological information is available at temporal resolutions of 1 minute from the SMOS, we append the surface values to the range bin in the profile that corresponds to the surface. No effort is made to smooth the transitions between the observations from different sources, and these transitions are often quite noticeable in the time series plots. Account is kept, however, of what information contributes to a particular thermodynamic profile.

Since a well-known upper tropospheric dry bias exists in the ARM radiosonde data (Revercomb et al, 2003, Turner et al., 2002), we apply the correction scheme reported by Miloshevich et al. (2001). We then examine the MMCR data to identify where in each profile cloud is observed. In the cloudy bins, we force the relative humidity to be 100%. In regions warmer than freezing, we use the equilibrium vapor pressure with respect to pure water and at temperatures colder than 243 K we use the relative humidity with respect to pure ice. In the intermediate temperatures, a linear combination of the relative humidity with respect to ice and water is used. While the absolute value of the corrected mixing ratio profiles are questionable (Soden et al., 2004), we rescale the mixing ratio profile based on the one-minute averaged MWR-derived water vapor

path. This straightforward technique assumes the shape of the mixing ratio profile created by the linear interpolation procedure, the dry-bias correction, and the cloud occurrence correction faithfully represents the vertical distribution of water vapor in the column. The adjusted mixing ratio profile is converted to a weighting function and the MWR column integrated water vapor is distributed vertically according to this weighting function. This somewhat elaborate procedure is necessary due to the sensitivity of the longwave radiation to the vertical distribution of water vapor in the troposphere.

The evolution of the moisture and temperature from 1-3 March is shown in Figure 4. The launch times of the 3-hourly soundings are shown as vertical lines in the height-time cross sections while the sounding data are shown compared to the Merged Sounding interpolation for each. We find the interpolated temperature is essentially indistinguishable from the measurement while the humidity diverges slightly from the measurement in the upper troposphere of several soundings. This apparent discrepancy is due to the fact that the sounding takes 30-40 minutes generally to reach the upper troposphere and we are comparing the Merged Sounding at the time of the launch, thus the small time offset between the actual measurement time and the interpolation time is enough to cause this difference in a rapidly changing water vapor field. While the humidity profiles shown in Figure 4b have not been scaled by the MWR vapor path, the values in the height time cross section have been. On the humidity cross section, we also show by the black symbols along the top of the diagram the diagnosis of precipitation using the empirical MWR technique described above. Besides the periods when the MWR is wet, two periods of anomalous humidity in the upper troposphere occurred near 21-22 UTC on 3/2 and 9-10 UTC on 3/3 in heavy cloud cover just after a period of light precipitation. The humidity sensor on the

RS90 Sonde did not recover after leaving the cloud tops and continued to report high humidity into the stratosphere. This problem is reasonably well documented but is not captured by any quality control procedures currently in place.

Millimeter Cloud Radar (MMCR)

Since clouds are a key component of this observation-based strategy, profiles of cloud properties are needed as a function of height and time. The active cloud profiling instruments at the SCF are the millimeter cloud radar (MMCR), micropulse lidar (MPL) and the Raman lidar (RL). We use the MMCR primarily in this work. The MMCR is a vertically pointing Doppler radar operating at 35 GHz (Moran et al., 1998). The theory of cloud detection by millimeter radar can be found in Doviak and Zrnic, (1993) and Clothiaux et al. (1995) and, for the MMCR in particular in Clothiaux et al., (1999).

The four MMCR data collection modes, optimized for various cloud types, run consecutively in a 36 s cycle. The cloud vertical profiles must be reconstructed from the modes in order to take advantage of the full capability of the MMCR data stream. Before this is accomplished, however, the significant radar echos in the MMCR data profiles must be identified. Following the techniques described in Clothiaux et al. (1995) we have implemented cloud masking routines to identify this significant return in the MMCR profiles and then merge the modes into a single description of the Doppler moments in the vertical column. When merging the profiles, we depart from the technique described by Clothiaux et al. (2000) in that we do not perform interpolation to a 9 s temporal grid (the temporal spacing of the individual modes), instead we

estimate the most reasonable measurements for a given 90 m vertical bin from one of the modes during the 36 s cycle and assign the three Doppler moment measurements from that particular mode to that bin. The temporal resolution of the merged radar Doppler moments product that we construct is then 36 s. Throughout the remainder of this work we will identify this product as the "Merged Moments". Significant radar echoes from clouds are distinguished from insect and precipitation echoes in the boundary layer by using cloud base measurements recorded by ceilometers. The key differences between this radar product and the Active Remote Sensing by Clouds (ARSCL) product created operationally by ARM is the factor of 4 reduction in size of the data and a consistency between the radar reflectivity and the other two Doppler moments (velocity and spectral width).

Acknowledgements

Funding for this work was provided by the Environmental Science Division of the U.S. Department of Energy (Grant DE-FG0398ER657). Data were obtained from the Atmospheric Radiation Measurement Program sponsored by the U. S. Department of Energy, Office of Science, Office of Biological and Environmental Research, Environmental Science Division. S. K. is supported by a NASA grant of the Clouds and the Earth's Radiant Energy System (CERES) project grant (NNL04AA26G).

References:

Ackerman, T. P., and G. M. Stokes. The Atmospheric Radiation Measurement Program. *Physics Today* 56: 38 – 45, 2003.

Atlas, D., S.Y. Matrosov, A.J. Heymsfield, M.-D. Chou, and D.B. Wolff, Radar and radiation properties of ice clouds. *J. Appl. Meteorol.*, 34, 2329-2345, 1995.

Barnard J. C., J. C. Doran, S. Zhong, and C. N. Long, A comparison of cloud properties at Barrow and SHEBA during the Summer of 1998, Proc. 11-th Atmospheric Radiation Measurement (ARM) Science Team Meeting. March 2000, Atlanta, 2001.

Clothiaux, E. E., M. A. Miller, B. A. Albrecth, T. P. Ackerman, J. Verlinde, D. M. Babb, R. M. Peters, W. J. Syrett, 1995: An evaluation of a 94 GHz radar for remote sensing of cloud properties. *J. Atmos. Oceanic Technol.,* **12,** 281-229, 1995.

Clothiaux, E. E., K. P. Moran, B. E. Martner, T. P. Ackerman, G. G. Mace, T. Uttah, J. H. Mather, K. B. Widener, M. A. Miller, D. J. Rodriguez. The Atmospheric Radiation Measurement program cloud radars: Operational modes. *J. Atmos. Oceanic. Technol.,* **16,** 819-827, 1999.

Clothiaux, E. E., T. P. Ackerman, G. G. Mace, K. P. Moran, R. T. Marchand, M. A. Miller, B. E. Martner. Objective determination of cloud heights and radar reflectivities using a combination of active remote sensors at the ARM CART sites. *J. Appl. Meteor.,* **39,** 645-665, 2000.

Dong, X., G. G. Mace. Profiles of low-level stratus cloud microphysics deduced from ground-based measurements. *J. Atmos. Oceanic Technol.,* 20, 45-53, 2003.

Dong., X., P. Minnis, G. G. Mace, W. L. Smith, M. Poellot, R. T. Marchand, A. D. Rapp. Comparison of stratus cloud properties derived from surface, GOES, and aircraft data during the March 2000 ARM cloud IOP. *J. Atmos. Sci.,* **59,** 3265-3284, 2002.

Doviak, R. J., and D. S. Zrnic. *Doppler Radar and Weather Observations.* Second Edition. Academic Press, San Diego, California, 1993.

Frisch, A. C., W. Fairall, and J. B. Snider, 1995: Measurement of stratus cloud and drizzle parameters in ASTEX with a K-band Doppler radar and a microwave radiometer, *J. Atmos. Sci.,* **52,** 2788-2799, 1995.

Frisch, A. C., G. Feingold, W. Fairall, and T. Uttal. On cloud radar and microwave radiometer measurements of stratus cloud liquid water profiles, *J. Geophys. Res.*, **103,** 23195-23197, 1998.

Fu, Q., 1996: An accurate parameterization of the solar radiative properties of cirrus clouds for climate models. *J. Climate,* 9, 2058-2082.

Fu, Q., P. Yang, and W. B. Sun, An accurate parameterization of the infrared radiative properties of cirrus clouds for climate models, *J. Climate,* 9, 2223-2237, 1998.

Fu, Qiang, Y, Ping Sun, WB, An accurate parameterization of the infrared radiative properties of cirrus clouds for climate models

Fu, Qiang; Yang, Ping; Sun, WB, Journal of Climate, Boston, MA. Vol. 11, no. 9, pp. 2223-2237. 1998.

Heymsfield, A. J. Ice crystal terminal velocities. *J. Atmos. Sci.,* **29,** 1348-1357, 1972.

Heymsfield, A. J., Precipitation development in stratiform ice clouds. *J. Atmos. Sci.,* **34,** 367-381, 1977.

Heymsfield, A. J., and C. M. R. Platt, A parameterization of the particle size spectrum of ice cloud in terms of the ambient temperature and ice water content. *J. Atmos. Sci.,* **41,** 846-855, 1984.

Kato, S. , G. L. Smith, and H. W. Barker, 2001: Gamma-weighted discrete ordinate two-stream approximation for computation of domain-averaged solar irradiance. J. Amos. Sci., 58, 3797-3803

Kato, S., T. P. Ackerman, J. H. Mather, and E. E. Clothiaux, 1999: The k-distribution method and correlated-k approximation for a Shortwave Radiative Transfer Model, J. Quant.Spectrosc. Radiat. Transfer, 62, 109-121

Khaiyer, M. M., A. D. Rapp, P. Minnis, D. R. Doelling, W. L. Smith, Jr., L. Nguyen, M. L. Nordeen, and Q. Min, 2002: Evaluation of a 5-year cloud and radiative property dataset derived from GOES-8 data over the southern Great Plains. *Proc. 12th ARM Science Team Meeting*, April 8-12, St. Petersburg, FL, 14 pp. Available at http://www.arm.gov/docs/documents/technical/conf_0204/khaiyer-mm.pdf.

Kiehl, J. J. Hack, G. B. Bonan, B. A. Boville, D. L. Williamson, and P. J. Rasch, 1998: The National Center for Atmospheric Research Community Climate Model: CCM3. J. Climate, 11, 1131-1149.

Liu, C. and A. J. Illingworth, 2000; Toward more accurate retrievals of ice water content from radar measurements of clouds. *J. Applied Meteorol.,* 39, 1130-1146.

Lau, N-C. and M.W. Crane, 1995; A satellite view of the synoptic scale organization of cloud properties in midlatitude and tropical cloud systems, *Mon. Wea. Rev.*, 123, 1984-2006.

Liljegren, J. C., E. E. Clothiaux, G. G. Mace, S. Kato, and X. Dong, A new retrieval for cloud liquid water path using a ground-based microwave radiometer and measurements of cloud temperature, *J. Geophys. Res.,* 106 (13) 14485-14500, 2001.

Liou K. N., Analytic two-stream and four-stream solutions for radiative transfer, *J. Atmos. Sci.,* 31, 1473-1475, 1974.

Long, C. N., and T. P. Ackerman, Identification of clear skies from broadband pyranometer measurements and calculation of downwelling shortwave cloud effects, *J. Geophys. Res.,* 105, 15609-15626, 2000.

Mace G. G., E. E. Clothiaux, and T. P. Ackerman, 2001: The composite characteristics of cirrus clouds; Bulk properties revealed by 1-year of continuous cloud radar data, *J. Climate*, 14, 2185-2203.

Mace G. G., K. Sassen. A constrained algorithm for retrieval of stratocumulus cloud properties using solar radiation, microwave radiometer and millimeter cloud radar data, *J. Geophys. Res.* 105, 29,099-29,108, 2000.

Mace, G. G., T. P. Ackerman, P. Minnis and D. F. Young: Cirrus layer microphysical properties derived from surface-based millimeter radar and infrared interferometer data. *J. Geophys. Res.,* 103, 23,207-23216, 1998.

Mace G. G A. J. Heymsfield, M. R. Poellot, 2002: On retrieving the microphysical properties of cirrus using millimeter wave Doppler moments data, *J. Geophys. Res.* 107.

Mace, G. G., D. O'C. Starr, T. P. Ackerman and P. Minnis, 1995: Examination of coupling between an upper tropospheric cloud system and synoptic scale dynamics diagnosed from wind profiler and radiosonde data. *J. Atmos. Sci*., 52, 4094-4127

Marchand, R., T. Ackerman, E. R. Westwater, S. A. Clough, K. Cady-Pereira, and J. C. Liljegren. An assessment of microwave absorption model and retrievals of cloud liquid water using clear-sky data, *J. Geophys. Res.,* 108 (24), DOI 1.1029/2003JD003843, 2003.

Matrosov, S.Y., B.W. Orr, R.A. Kropfli, and J.B. Snider, Retrieval of vertical profiles of cirrus cloud microphysical parameters from Doppler radar and infrared radiometer measurements, *J. Appl. Meteor*., 33, 617-626, 1994.

Miloshevich, L. M., H. Vomel, A. Paukkunen, A. J. Heymsfield, and S. J. Oltmans. Characterization and correction of relative humidity measurements from Vaisala Rs80A radiosondes at cold temperatures. *J. Atmos. Oceanic. Technol.,* **18,** 135-155.

Min, Q.-L., and L. C. Harrison, Cloud properties derived from surface MFRSR measurements and comparison with GOES results at the ARM SGP site, *Geophys. Res. Lett., 23*, 1641, 1996a.

Min, Q.-L., and L. C. Harrison, An Adjoint Formulation of the Radiative Transfer Method, *J. Geophys. Res., 101*, 1635, 1996b.

Min, Q.-L., and L. C. Harrison, Comparison of model-predicted total shortwave with measurements under overcast cloud conditions, *in Proceedings of the eighth ARM Science team meeting*, Tucson, 493, 1998

Min, Q.-L., M. Duan, and R. Marchand, Validation of surface retrieved cloud optical properties with in situ measurementsat the Atmospheric Radiation Measurement Program (ARM) South Great Plains site, J. Geophys. Res., 108(D17), 4547,doi:10.1029/2003JD003385, 2003.

Min, Q.-L., E. Joseph, and M. Duan, Retrievals of thin cloud optical depth from a multifilter rotating shadowband radiometer, J. Geophys. Res., 109, D02201, doi:10.1029/2003JD003964, 2004a.

Min, Q.-L., P. Minnis, and M. Khaiyer, Comparison of cirrus optical depths derived from GOES 8 and surface measurements, J. Geophys. Res., 109, D15207, doi:10.1029/2003JD004390, 2004b.

Minnis, P., P. W. Heck, and D. F. Young, 1993: Inference of cirrus cloud properties using satellite-observed visible and infrared radiances, Part II: Verification of theoretical cirrus radiative properties. *J. Atmos. Sci.*, **50**, 1305-1322.

Minnis, P., L. Nguyen, D. R. Doelling, D. F. Young, W. F. Miller, and D. P. Kratz, 2002: Rapid calibration of operational and research meteorological satellite imagers, Part I: Evaluation of research satellite visible channels as references. *J. Atmos. Oceanic Technol.*, **19**, 1233-1249.

Minnis, P. and W. L. Smith, Jr., 1998: Cloud and radiative fields derived from GOES-8 during SUCCESS and the ARM-UAV Spring 1996 Flight Series. *Geophys. Res. Lett.*, **25**, 1113-1116.

Minnis, P., W. L. Smith, Jr., D. P. Garber, J. K. Ayers, and D. R. Doelling, 1995: Cloud properties derived From GOES-7 for the Spring 1994 ARM Intensive Observing Period using Version 1.0.0 of the ARM satellite data analysis program. *NASA RP 1366*, 59 pp.

Mitchell, D. L., Use of mass- and area-dimensional power laws for determining precipitation particle terminal velocities. *J. Atmos. Sci.,* **53,** 1710-1723, 1996.

Mlawer, E. J., S. J. Taubman, P. D. Brown, M. J., Iacono, S. A. Clough, Radiative transfer for inhomogeneous atmospheres: RRTM, a validated correlated-k model for the longwave, *J. Geophys. Res.,* 102, 16663-16682, 1997.

Ockert-Bell, M. E., and D. L. Hartmann, 1992: The effect of cloud type on earth's energy balance: Results for selected regions. *J. Climate,* **5,** 1157–1171.

Peixoto, J. P., and A. Oort, 1993: *The Physics of Climate,* American Institute of Physics, New York, 520 pp.

Randall, D. A., B. A. Albrecht, S. K. Cox, P. Minnis, W. Rossow, and D. Starr, 1995: On FIRE at ten. *Adv. Geophys.,* **38,** 37–177.

Randall, D. A., 1995: Editorial; Atlantic Stratocumulus Transition Experiment. *J. Atmos. Sci.,* **52,** 2705.

Revercomb, H. E., et al., The atmospheric radiation measurement program's water vapor intensive observation periods: Overview, initial accomplishments, and future challenges, *Bull. Am. Meteorol. Soc.,* **84,** 217-236, 2003.

Rossow, W. B., and T.-C. Zhang. Calculation of surface and top of atmosphere radiative fluxes from physical quantities based on ISCCP data sets 2. validation and first results. J. Geophys. Res., 100, 1167-1197, 1995.

Rossow, W. B., and R. A. Schiffer: Advances in understanding clouds from ISCCP. *Bull. Amer. Meteor. Soc.,* 80, 2261-2288, 1999.

Slingo, J. M., 1989: A GCM parameterization for the shortwave radiative properties of water clouds. J. Atmos. Sci., 46, 1419-1427.

Stephens, G. L.. Cloud feedbacks in the climate system: A critical review. *J. Climate,* In Press, 2004.

Soden, B. J., D. D. Turner, B. M. Lesht, and L. M. Miloshevich, An analysis of satellite, radiosonde, and lidar observations of upper tropospheric water vapor from the Atmospheric Radiation Measurement Program. *J. Geophys. Res.,* **109,** D04105, doi:10,1029/2003JD003828, 2004

Stokes, G. M, and S. E. Schwartz, The atmospheric radiation measurement (ARM) program: Programmatic background and design of the cloud and radiation testbed. *Bull. Amer. Meteor. Soc.,* 75, 1201-1221, 1994.

Stephens, G. L., 1995: Editorial; The First ISCCP Regional Experiment Intensive Field Observations II., *J. Atmos. Sci.,* **52.** 4041.

Stephens, G. L., 1994: *Remote Sensing of the Lower Atmosphere; An Introduction.* Oxford University Press, New York. 523pp.

Toon, O. B., C. P. McKay, T. P. Ackerman, K. Santhanam, Rapid calculation of radiative heating rates and photodissociation rates in inhomogeneous multiple scattering atmospheres, *J. Geophys. Res.,* 94 (D13), 16287-16301, 1989.

Turner, D. D., B. M. Lesht, S. A. Clough, J. C. Liljegren, H. E. Revercomb, and D. C. Tobin. Dry bias and variability in Vaisala radiosondes: The ARM experience, *J. Atmos. Oceanic. Technol.,* **20,** 117-132, 2003.

Twohy, C. H., A. J. Schanot, and W. A. Cooper. Measurement of condensed water content in liquid and ice clouds using an airborne counterflow virtual impactor. *J. Atmos. Oceanic. Techno.,* **14,** 197-202., 1997.

Webb, M., C. Senior, S. Bony and J. J Morcrette, Combining ERBE and ISCCP data to assess clouds in the Hadley Centre, ECMWF and LMD atmospheric climate models. *Clim. Dyn., 17*, 905-922, 2001.

Wielicki, B. A., Barkstrom, B. R., Baum, B. A., Charlock, T. P., Green, R. N., Kratz, D. P., Lee, R. B., Minnis, P., Smith, G. L., Young, D. F.; Cess, R. D.; Coakley, J. A.; Crommelynck, D. A. H.; Donner, L.; Kandel, R.; King, M. D.; Miller, A. J.; Ramanathan, V.; Randall, D. A.; Stowe, L. L.; and Welch, R. M., Clouds and the Earth's Radiant Energy System (CERES): Algorithm Overview. *IEEE Transactions on Geoscience and Remote Sensing*, **36**, July 1998, pp. 1127-1141.

Webster, P. J., and G. L. Stephens. Cloud-radiation interaction and the climate problem, in *The Global Climate,* edited by J. T. Houghton, pp. 63-78, Cambridge University Press, new York, 1984.

Zhang, M. H. and Coauthors, Comparing clouds and their seasonal variations in 10 atmospheric general circulation models with satellite measurements. *J. Geophys. Res.* In Press, 2004.

Table 1. Coefficients of the regression relationship (Equation 1) relating Z_e (mm^6 m^{-3}), V_d (m s^{-1}), and T (K) to IWC (g cm^{-3})

a	*b*	*c*
-1.52e-8	8.76e-8	2.28e-10

Table 2. Comparison statistics of the parameterized versus observed *IWC* derived from Equation 1 and Table 1 and shown in Figure 6.

Bias (g m^{-3})	Median Fractional Error	Slope of Linear Fit	Intercept of Linear Fit (g m^{-3})	Correlation Coefficient	Normal Deviation (g m^{-3})	Number of Obs
0.0002	0.33	0.95	0.0033	0.83	0.0034	1560

Table 4. Comparison of calculated to observed fluxes (Observations are in brackets) at the times shown in Figure 8. With the exception of albedo, the units are W m^{-2}. The firs number in each cell is the calculated value.

Time	TOA Albedo	TOA OLR (W m^{-2})	Sfc IR down (W m^{-2})	Sfc Solar down (W m^{-2})
2245 UTC 3/1	0.39 [0.40]	188 [202]	301 [305]	242 [229]
1700 UTC 3/3	0.55 [0.50]	215 [200]	240 [220]	325 [330]

Table 3. Summary of the optical depth comparison between the MFRSR value and CPC derived values for the year 2000. The second row is the same as the first except referenced to the $\log_{10}$ of the optical depths.

Mean Fractional Bias	Median Fractional Bias	Fractional RMS Difference	Slope of Linear Fit	Intercept of Linear Fit	Correlation Coefficient	Normal Deviation	Number of Obs
0.46	0.10	0.60	0.86	0.79	0.89	0.20	1520
0.26	0.0	0.23	0.94	-0.01	0.88	0.09	1520

Table 5a Comparison statistics of TOA and surface radiation quantities calculated using the CPC technique with observations. At the surface we compare with ARM pyranometer and pyrgeometer measurements and at the TOA we compare with broadband fluxes derived from GOES radiances using the LBTM algorithm. Period covered is the entire year 2000. All fractional values are reported relative to the mean of the observations. Units of all nonfractional values are W m^{-2}. All broken and overcast nonprecipitating cloud scenes are included. See the text for definition of symbols.

		Median Fractional Difference	Fractional Offset	Correlation Coefficient	RMS Diff	Slope of Linear Fit	Intercept of Linear Fit	Mean Obs	Normal Deviation	Number of Obs
TOA	$S\uparrow_t$	0.16	0.06	0.84	78	0.7	98	373	61	1198
	$L\uparrow_t$	0.02	-0.02	0.92	13.2	0.88	46.	350.6	8.37	2059
	$CFC - NS_t$	0.28	-0.11	0.83	100	0.71	-53	-252	56.6	441
SFC	$S\_Frac\downarrow_s$	0.22	-0.01	0.79	0.18	0.67	0.19	0.53	0.54	1311
	$L\downarrow_s$	0.02	-0.01	0.91	12	0.84	59	342	9.2	1877
	$CFC - NS$	0.21	-0.03	0.88	95	0.81	-45	-271	39.6	634

Table 5b. As in Table 5a except only overcast scenes are included

		Median Fractional Difference	Fractional Offset	Correlation Coefficient	RMS Diff	Slope of Linear Fit	Intercept of Linear Fit	Mean Obs	Normal Deviation	Number of Obs
TOA	$S\uparrow_t$	0.12	0.08	0.90	68	0.72	99	419	65	419
	$L\uparrow_t$	0.06	0.06	0.89	13	0.89	11	180	11	857
	$CFC - NS_t$	0.20	-0.05	0.81	107	0.60	-81	-335	74	213
SFC	$S\_Frac\downarrow_s$	0.13	0.01	0.8	0.17	0.67	0.20	0.62	0.10	739
	$L\downarrow_s$	0.02	-0.01	0.90	11.5	0.82	64	344	8.7	994
	$CFC - NS$	0.14	-0.05	0.84	76	0.84	-37	-330	38	304

Table 6. Statistics of the comparison between ARM CPC CTP and Tau with results from LBTM and ISCCP. The ISCCP data are averaged in 250 km and 100 km boxes centered on ARM SGP while the ICARUS statistics are from the nearest pixel. Statistics are compiled over the year 2000 using the comparison criteria described in section 2.2. All CTP quantities are shown in mb while the Tau values are computed relative to $\log_{10}$(Tau).

Comparison	Median Fractional Error	Bias	Slope of Linear Fit	Intercept of Linear Fit	Linear Correlation	Mean ARM	Mean ISCCP	Normal Deviation
CTP (CPC-ISCCP 250km)	0.14	8	0.71	129	0.90	459	467	78
CTP (ICARUS-ISCCP 250 km)	0.13	10	0.78	78	0.92	459	469	56
CTP (CPC-ISCCP 100 km)	0.13	15	0.8	83	0.92	472	487	58
CTP (ICARUS-ISCCP 100 km)	0.13	35	0.91	6	0.93	443	478	41
CTP (ARM-LBTM Nearest Pixel)	0.19	-31	0.63	198	0.79	475	445	100
CTP (ICARUS-LBTM Nearest Pixel)	0.13	22	0.86	50	0.90	475	497	35
CTP (ARM-LBTM 9 pixel avg)	0.19	-33	0.61	205	0.79	475	443	103
CTP (ICARUS-LBTM 9 pixel avg)	0.13	6	0.83	71	0.88	475	481	41
Log(Tau) (ARM-ISCCP 250 km)	0.20	-0.41	0.68	0.14	0.62	1.74	1.35	0.33
Log(Tau) (ARM-ISCCP 100 km)	0.20	-.42	0.68	0.14	0.57	1.74	1.32	0.41
Log(Tau) (ARM-LBTM Nearest Pixel)	0.22	-.47	0.71	0.04	0.65	1.73	1.26	0.34
Log(Tau) (ARM-LBTM 9 pixel avg)	0.24	-.43	0.69	0.11	0.68	1.74	1.33	0.31

Figure Captions

Figure 1. 500mb Heights (contours in m), abs vorticity (shaded), and horizontal wind (1 whole barb is 10 m/s) from the NCEP/NCAR reanalysis for the March 1-3, 2000 case study period. The date (month/day) and UTC time is shown on the lower left of each plot.

Figure 2. IR Geostationary satellite imagery of the ARM SGP region during the 3/1-3/3 case study period. The location of the ARM SCF is marked with a red square. State outlines are shown in green and latitude and longitude lines are shown in yellow. The color table is denoted in Kelvins.

Figure 3. MWR observations and wet window flag for the 3/1-3/3 case study period. The shaded regions denote periods where the empirical algorithm identifies a high likelihood that condensed liquid water on the instrument cover biased the MWR measurements.

Figure 4. Illustration of the thermodynamic fields derived from 3-hourly radiosondes, and MWR liquid water path during the 3/1-3/3 case study period. The top two plots show the interpolated values (dashed lines) compared to the soundings (solid) while the bottom two plots show the interpolated fields at 5 minute resolution. The heavy black symbols above the Relative Humidity height-time cross section show periods where the MWR liquid water path was likely contaminated by liquid water on the MWR cover (see Figure 3).

Figure 5. MMCR radar reflectivity of cloud layers during the 3/1-3/3 case study period. The red-shaded regions mark periods when the MWR cover was identified as likely wet, the gray shaded regions denote missing data, and the two black lines through the data at 2245 UTC on 3/1 and 1715 UTC on 3/3 denote profiles that are examined in more detail.

Figure 6. Comparison of IWC derived from the equation 1 regression relationship to CVI measurements of condensed water. See text for further details.

Figure 7. Condensed water derived from the CPC algorithm for the 3/1-3/3 case study period. In a) the total, liquid, and ice water paths are shown, b) the height-time section of total condensed water, c) the IWC, and d) the LWC. Light red shading denotes regions where the MWR is likely biased due to a wet cover. The LWC and total water should be viewed with caution during these times. Gray shaded areas denote missing data.

Figure 8. Illustration of the microphysical and radiative properties and the associated heating rates for two selected profiles during the 3/1-3/3 case study denoted by the thin black lines drawn vertically through the height-time section of radar reflectivity in Figure 5. The profiles are from 2245 UTC on 3/1 and at 17:00 on 3/3. For each profile, three figures (a-c and d-f) are shown depicting the condensed liquid (solid lines) and ice water (dashed lines) profiles in units of g m^{-3}, the extinction profiles due to the liquid (solid lines) and ice (dashed lines) in units of m^{-1} and the resulting solar (solid lines) and IR (dashed lines) heating rates in units of K day^{-1}.

Figure 9. Mean and standard deviation of cloud-induced heating rate profiles collected in vertical pressure bins (mb; abscissa) for the case study period from 3/1-3/3. The averaged values (depicted in units of K day^{-1}) are derived from instantaneous quantities calculated using 5-min averaged data. Shown are a) the solar heating rates, b) the IR heating rates, and c) the net heating rate. The uncertainties of these quantities are discussed in detail in Part II.

Figure 10. Comparison of total optical depth derived from the MFRSR (asterisk) and calculated (solid line) using the CPC technique. a) 3/1, b) 3/3. Time is shown in Julian day.

Figure 11. CPC optical depth compared to MFRSR Optical depth for a) 3/2000 and b) 3/2000-12/2000. In b) only the period between 17 UTC and 21 UTC was considered for MFRSR optical depth less than 5.

Figure 12. Comparison of derived fluxes (solid lines) with observations. In a) the calculated albedo is compared with values derived from GOES. In b) the surface solar flux is compared, and in c) the OLR (lower values) and the surface downwelling longwave (higher values) are shown.

Figure 13. Comparison of TOA and Surface cloudy fluxes with CPC calculations for all overcast scenes during the year 2000.

Figure 14. Cloud top pressure and total visible optical depth histograms from a) ISCCP in a 250 km domain centered on the SGP site, b) the nearest pixel of the LBTM algorithm to the ARM

SGP site, c) The ARM data CPC diagnostic, and d) the ICARUS simulation of the ISCCP algorithm using the ARM CPC information as input. The period covered is March 2000 during daylight hours.

Figure 15. Time series of (a) total condensed water diagnosed using the CPC technique, (b) cloud top pressure and (c) total cloud optical depth during 3/2000 diagnosed from the various sources as shown in the legend. The ISCCP values are shown as means and standard deviations derived in geographic domains centered on the ARM SGP site.

Figure 16. Comparison of ISCCP and LBTM quantities with ARM data. Shown in a) CTP from ISCCP compiled in a 100 km domain centered on the SGP site, b) as in a) except ISCCP is compared with ICARUS simulation using ARM data, c) LBTM from the pixel nearest the ARM SGP site, d) as in c) except LBTM is compared to the ICARUS simulation using ARM data, e) ISCCP optical depth is compared to the quantity derived from the ARM CPC diagnostic and f) as in e) except the Minnis nearest pixel optical depth is compared to ARM.

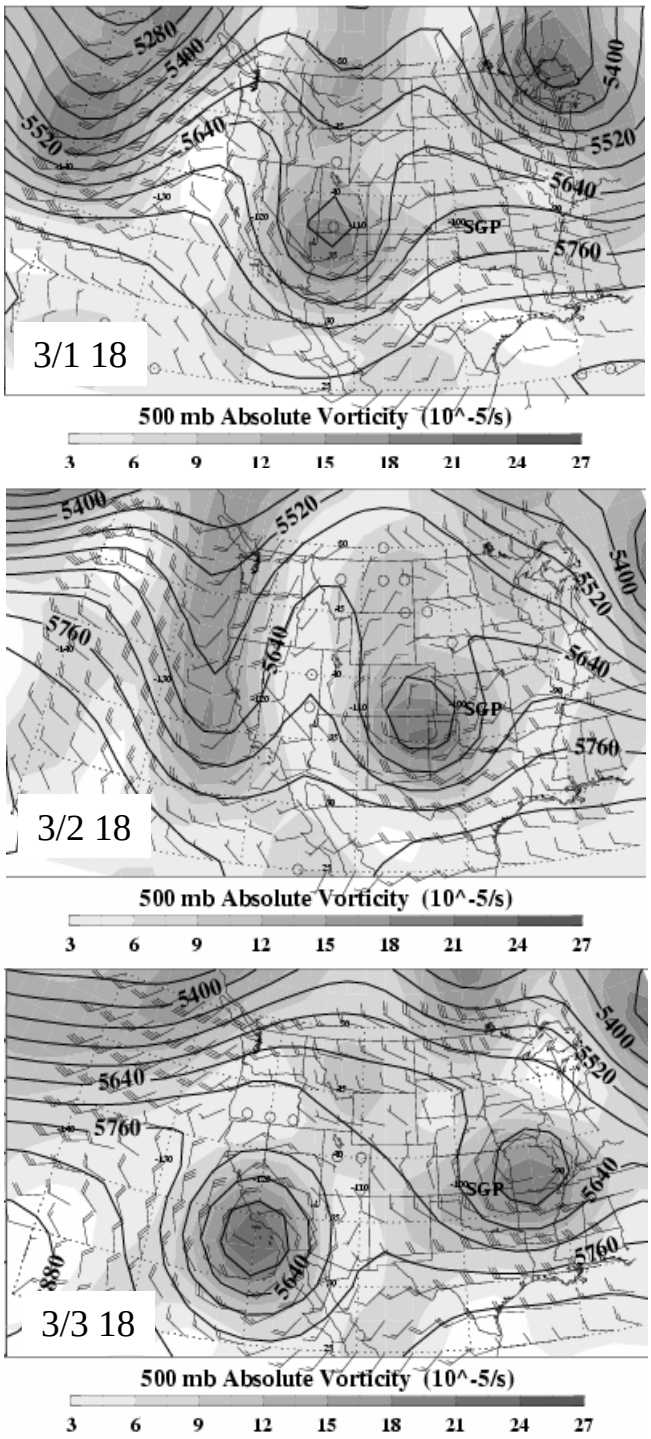

Figure 1. 500mb Heights (contours in m), abs vorticity (shaded), and horizontal wind (1 whole barb is 10 m/s) from the NCEP/NCAR reanalysis for the March 1-3, 2000 case study period. The date (month/day) and UTC time is shown on the lower left of each plot.

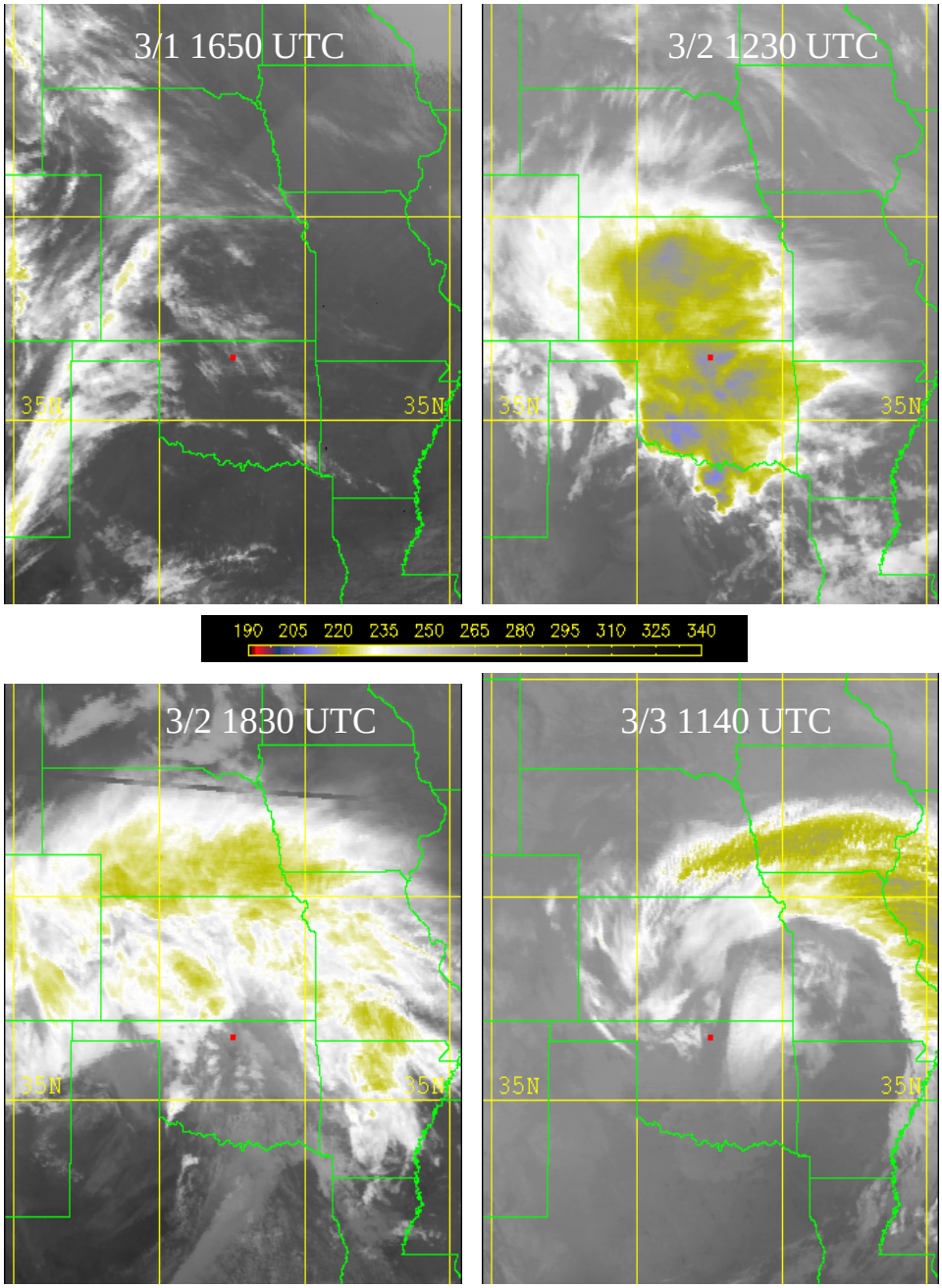

Figure 2. IR Geostationary satellite imagery of the ARM SGP region during the 3/1-3/3 case study period. The location of the ARM SCF is marked with a red square. State outlines are shown in green and latitude and longitude lines are shown in yellow. The color table is denoted in Kelvins.

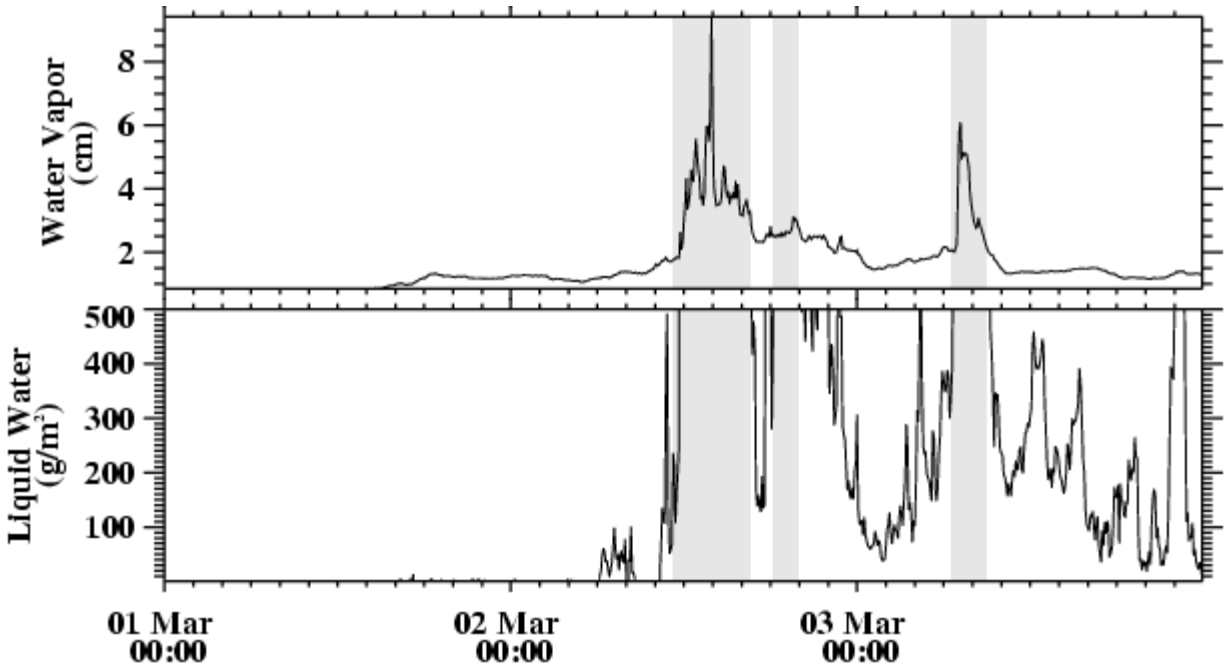

Figure 3. MWR observations and wet window flag for the 3/1-3/3 case study period. The shaded regions denote periods where the empirical algorithm identifies a high likelihood that condensed liquid water on the instrument cover biased the MWR measurements.

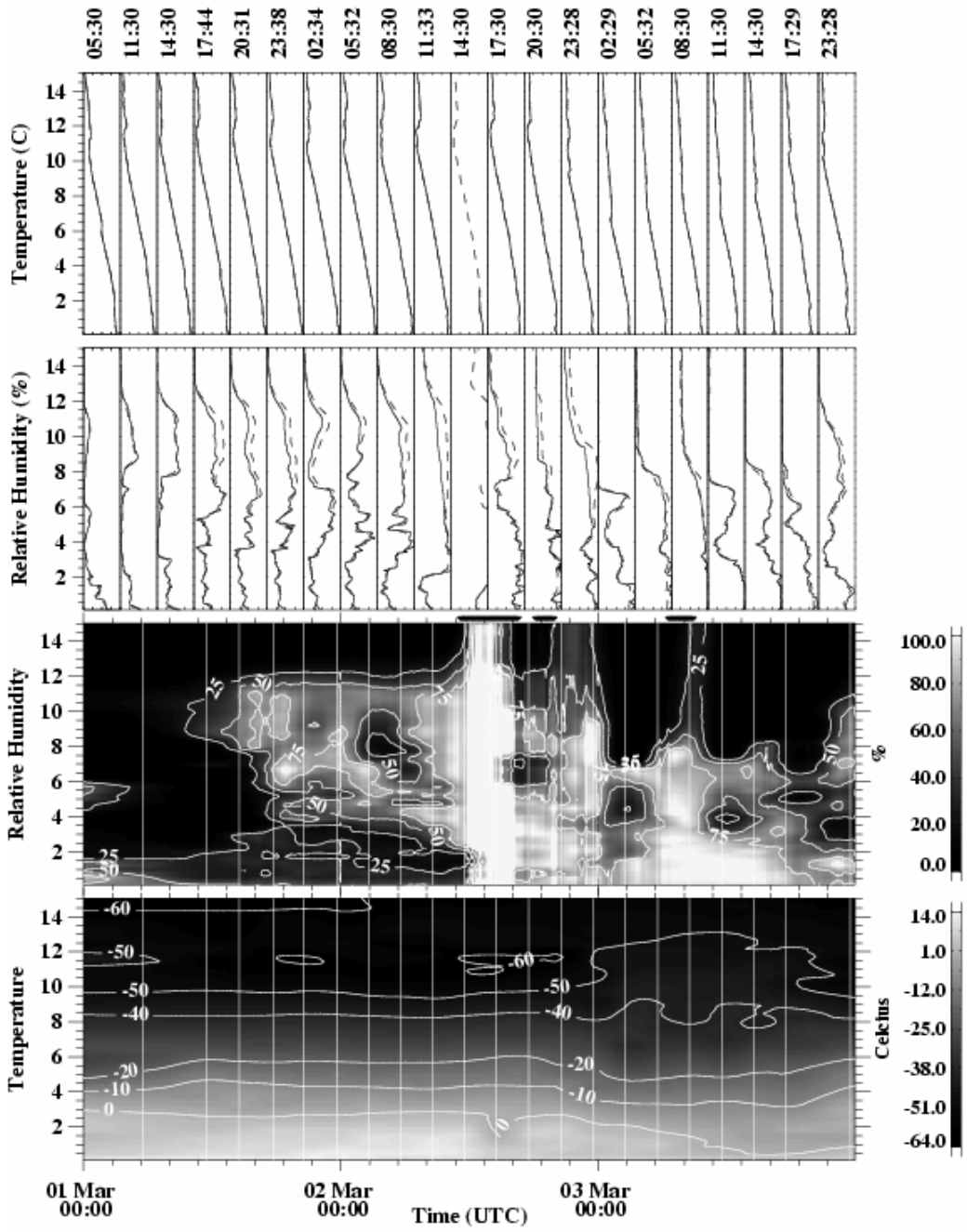

Figure 4. Illustration of the thermodynamic fields derived from 3-hourly radiosondes, and MWR liquid water path during the 3/1-3/3 case study period. The top two plots show the interpolated values (dashed lines) compared to the soundings (solid) while the bottom two plots show the interpolated fields at 5 minute resolution. The heavy black symbols above the Relative Humidity height-time cross section show periods where the MWR liquid water path was likely contaminated by liquid water on the MWR cover (see Figure 3).

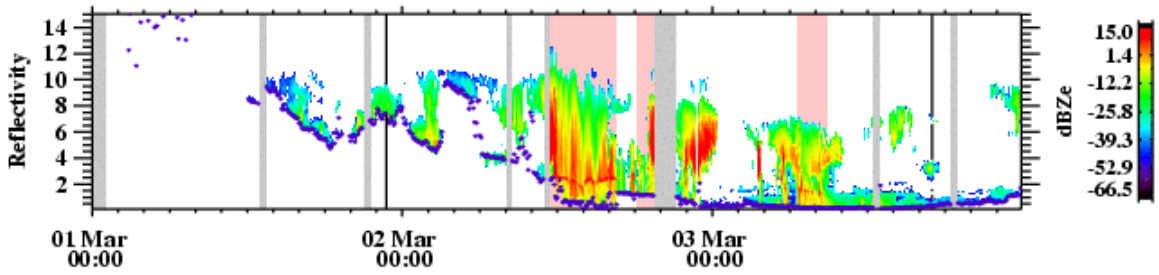

Figure 5. MMCR radar reflectivity of cloud layers during the 3/1-3/3 case study period. The red-shaded regions mark periods when the MWR cover was identified as likely wet, the gray shaded regions denote missing data, and the two black lines through the data at 2245 UTC on 3/1 and 1715 UTC on 3/3 denote profiles that are examined in more detail.

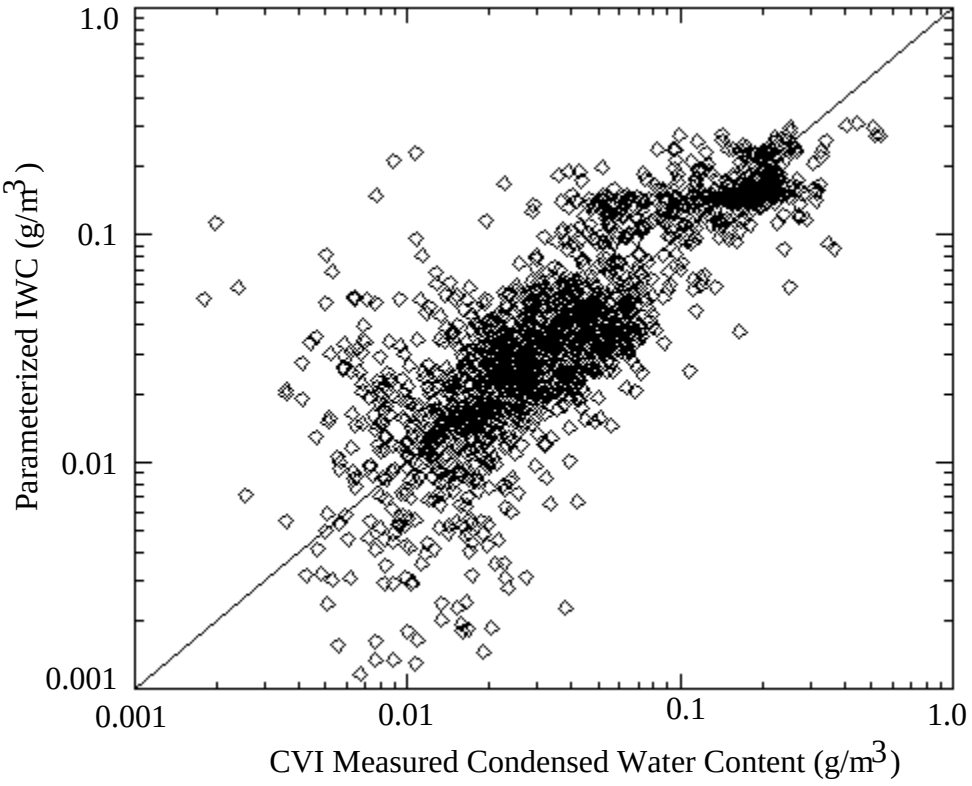

Figure 6. Comparison of IWC derived from the equation 1 regression relationship to CVI measurements of condensed water. See text for further details.

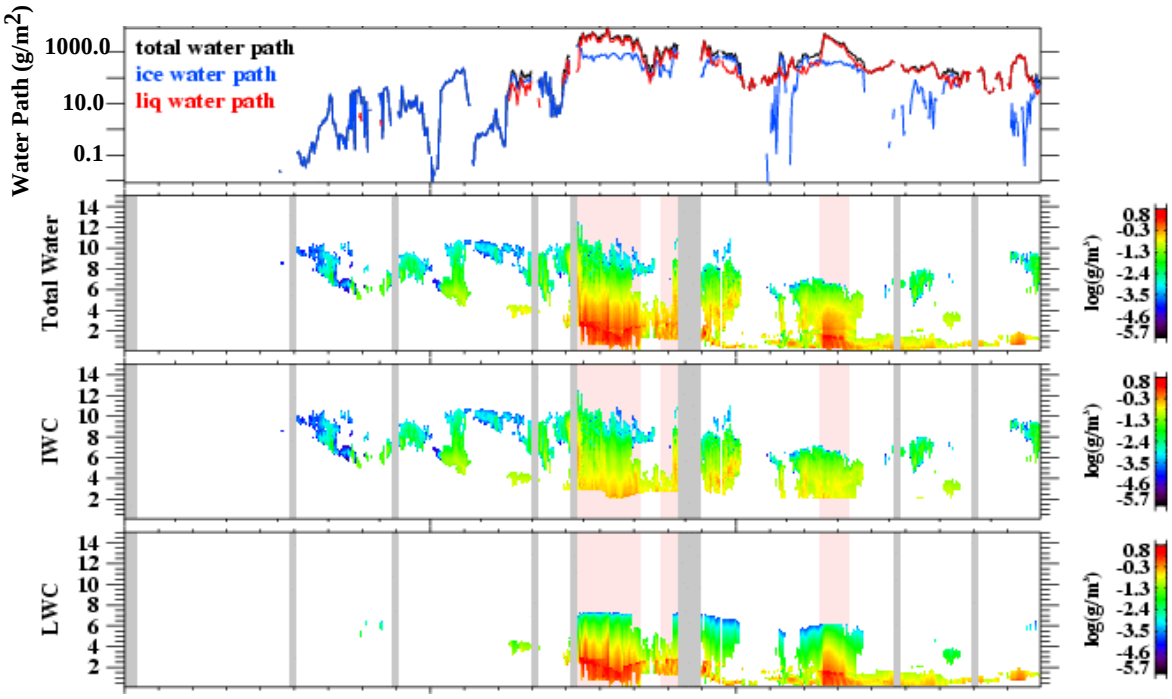

Figure 7. Condensed water derived from the CPC algorithm for the 3/1-3/3 case study period. In a) the total, liquid, and ice water paths are shown, b) the height-time section of total condensed water, c) the IWC, and d) the LWC. Light red shading denotes regions where the MWR is likely biased due to a wet cover. The LWC and total water should be viewed with caution during these times. Gray shaded areas denote missing data.

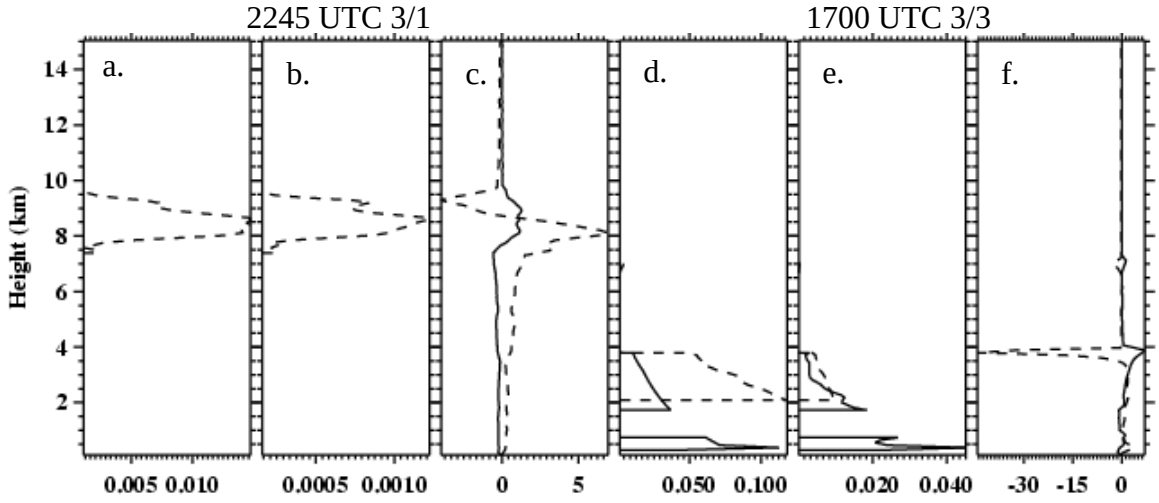

Figure 8. Illustration of the microphysical and radiative properties and the associated heating rates for two selected profiles during the 3/1-3/3 case study denoted by the thin black lines drawn vertically through the height-time section of radar reflectivity in Figure 5. The profiles are from 2245 UTC on 3/1 and at 17:00 on 3/3. For each profile, three figures (a-c and d-f) are shown depicting the condensed liquid (solid lines) and ice water (dashed lines) profiles in units of g m^{-3}, the extinction profiles due to the liquid (solid lines) and ice (dashed lines) in units of m^{-1} and the resulting solar (solid lines) and IR (dashed lines) heating rates in units of K day^{-1}.

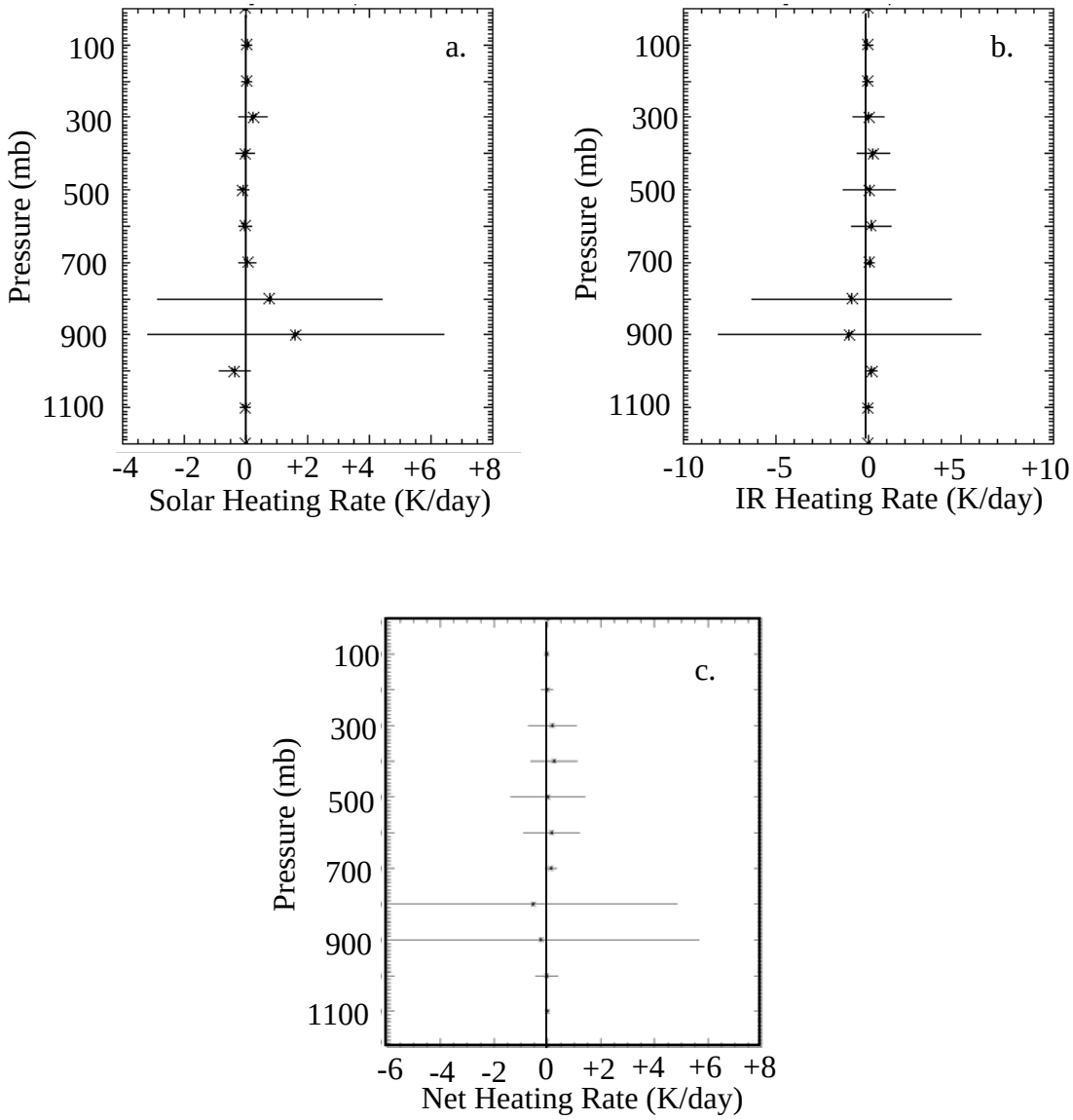

Figure 9. Mean and standard deviation of cloud-induced heating rate profiles collected in vertical pressure bins (mb; abscissa) for the case study period from 3/1-3/3. The averaged values (depicted in units of K day^{-1}) are derived from instantaneous quantities calculated using 5-min averaged data. Shown are a) the solar heating rates, b) the IR heating rates, and c) the net heating rate. The uncertainties of these quantities are discussed in detail in Part II.

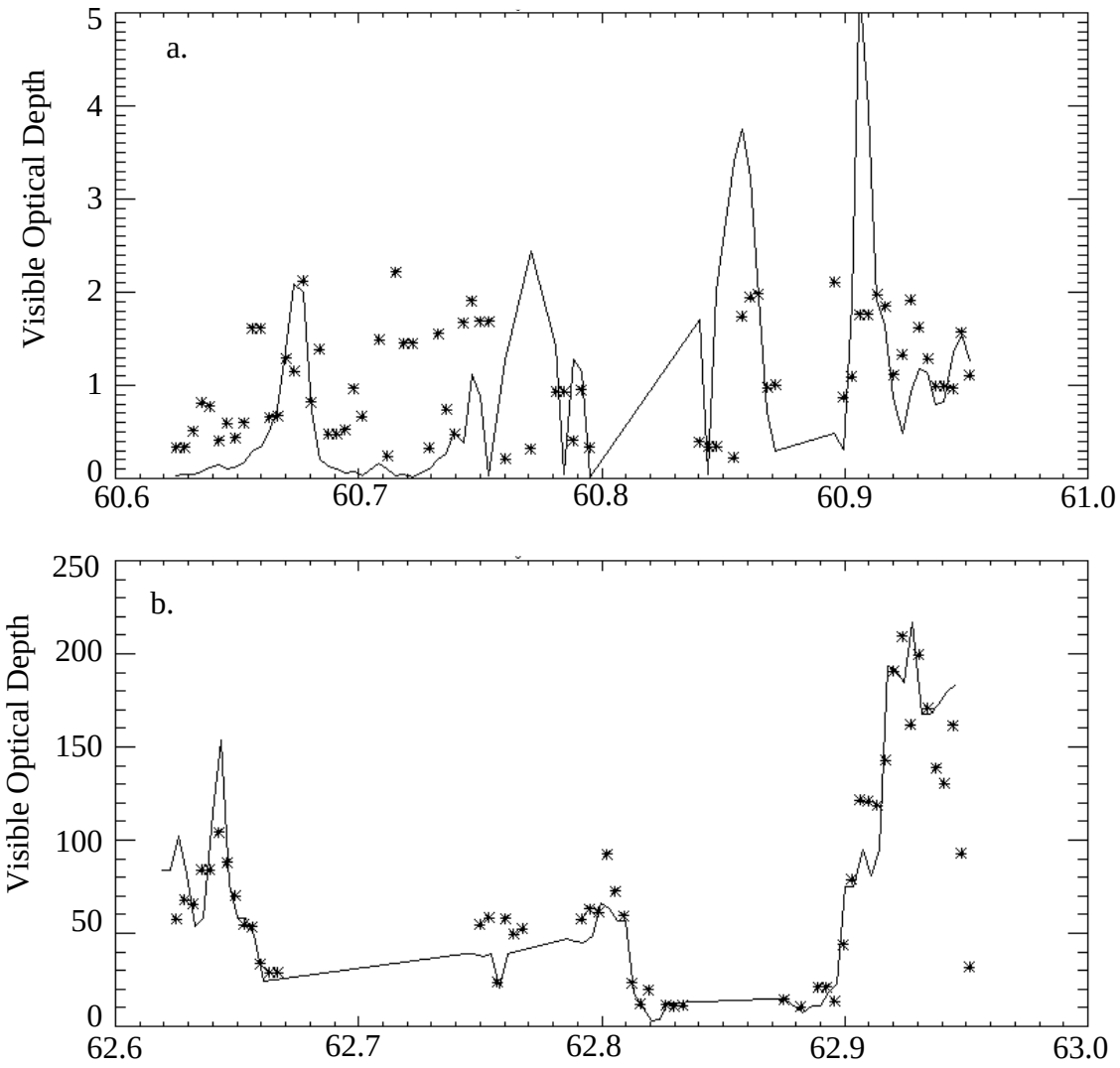

Figure 10. Comparison of total optical depth derived from the MFRSR (asterisk) and calculated (solid line) using the CPC technique. a) 3/1, b) 3/3. Time is shown in Julian day.

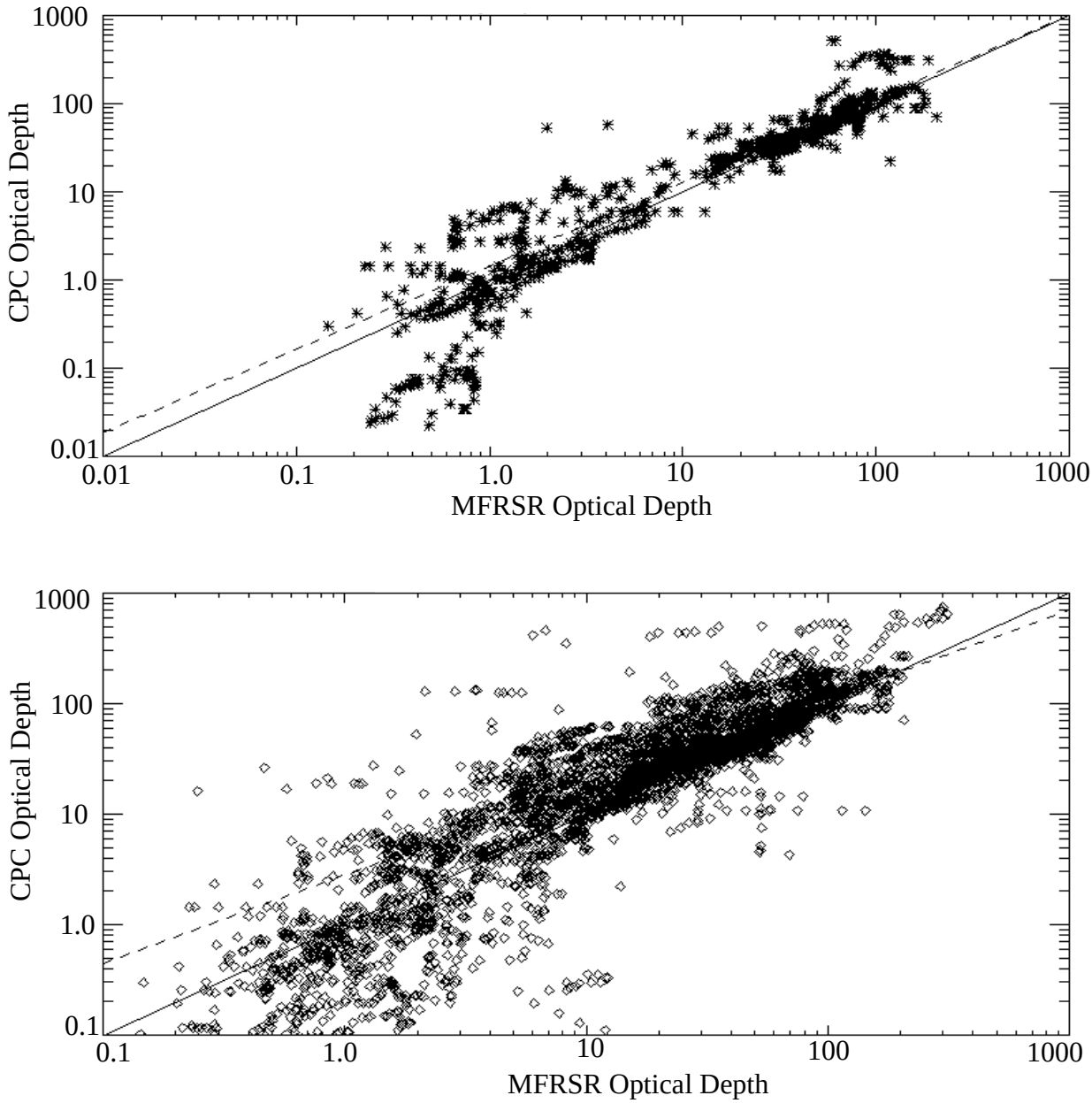

Figure 11. CPC optical depth compared to MFRSR Optical depth for a) 3/2000 and b) 3/2000-12/2000. In b) only the period between 17 UTC and 21 UTC was considered for MFRSR optical depth less than 5.

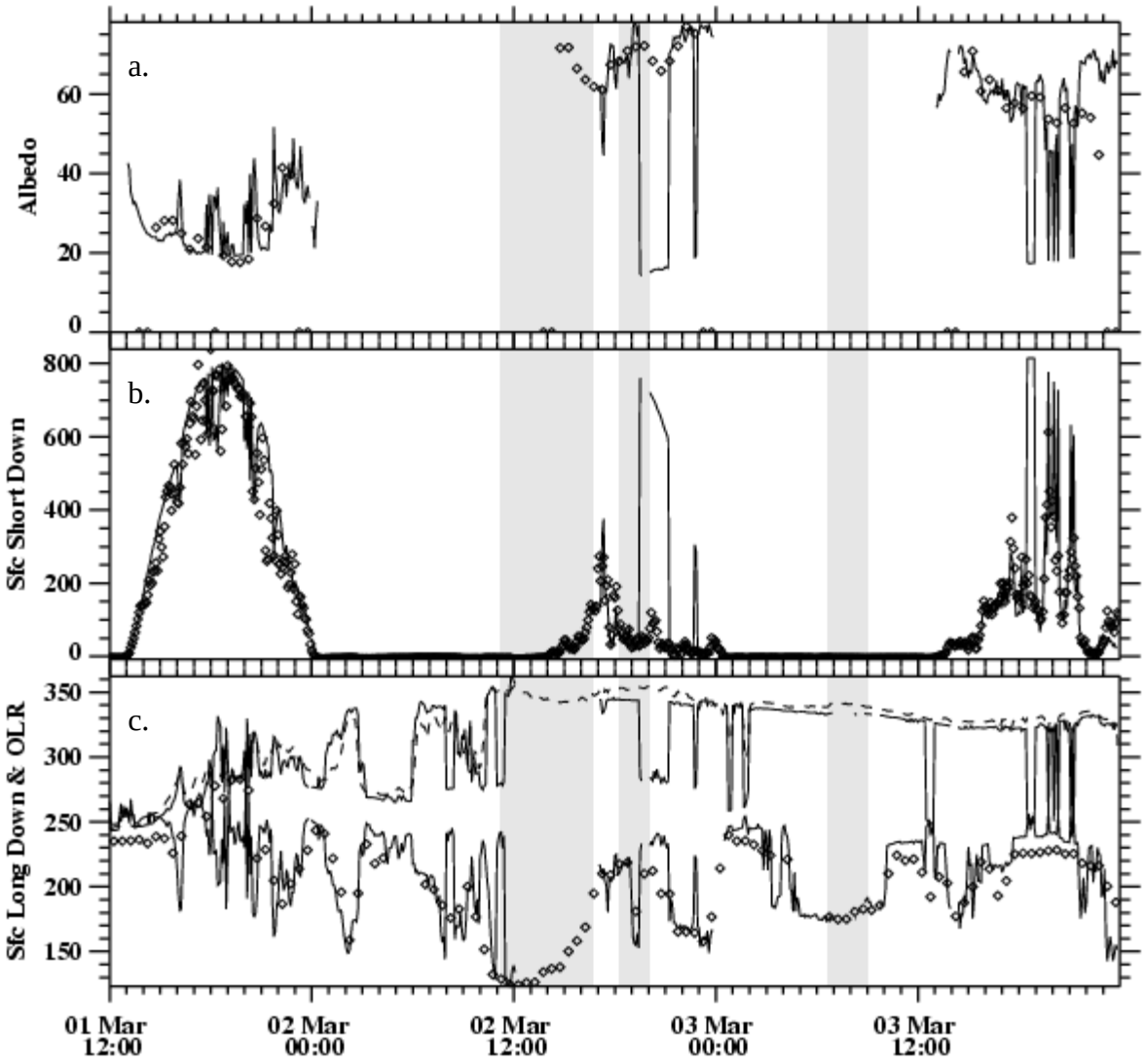

Figure 12. Comparison of derived fluxes (solid lines) with observations. In a) the calculated albedo is compared with values derived from GOES. In b) the surface solar flux is compared, and in c) the OLR (lower values) and the surface downwelling longwave (higher values) are shown.

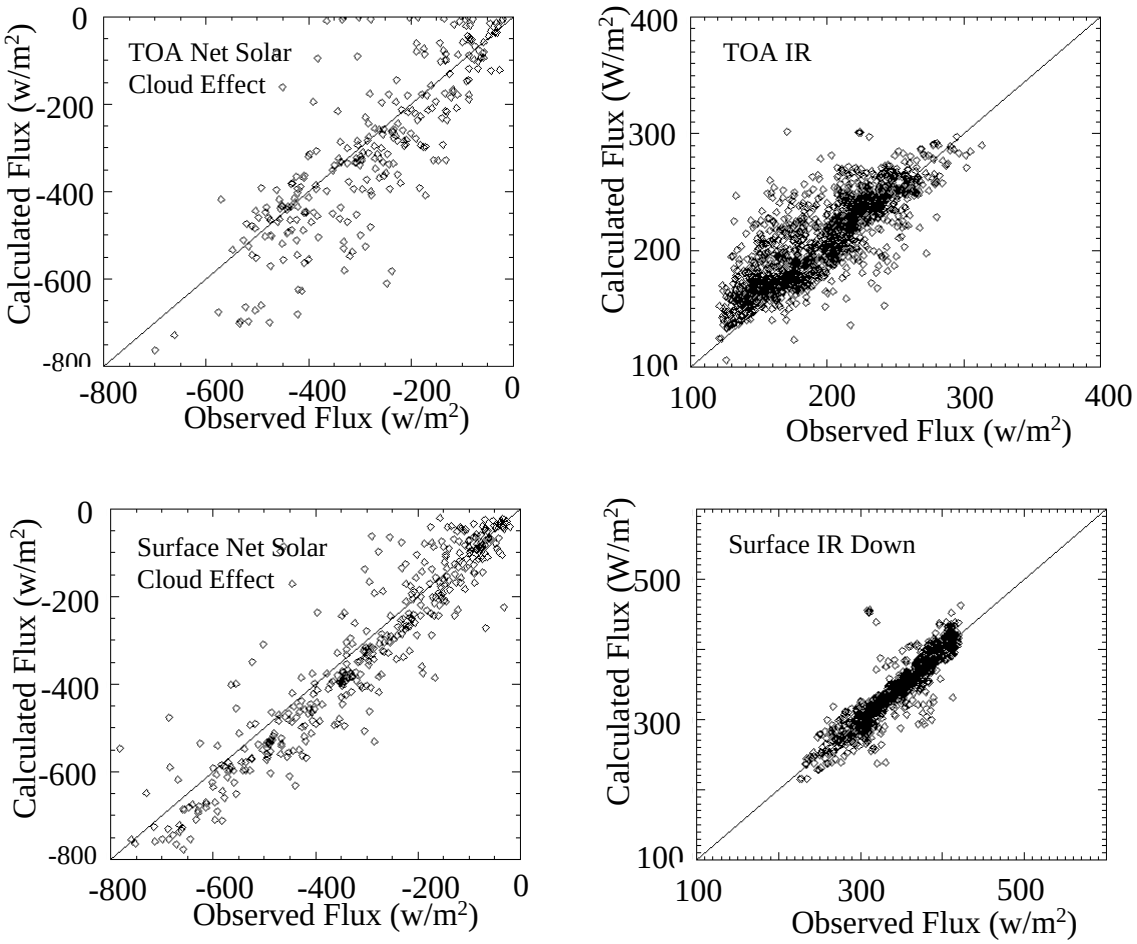

Figure 13. Comparison of TOA and Surface cloudy fluxes with CPC calculations for all overcast scenes during the year 2000.

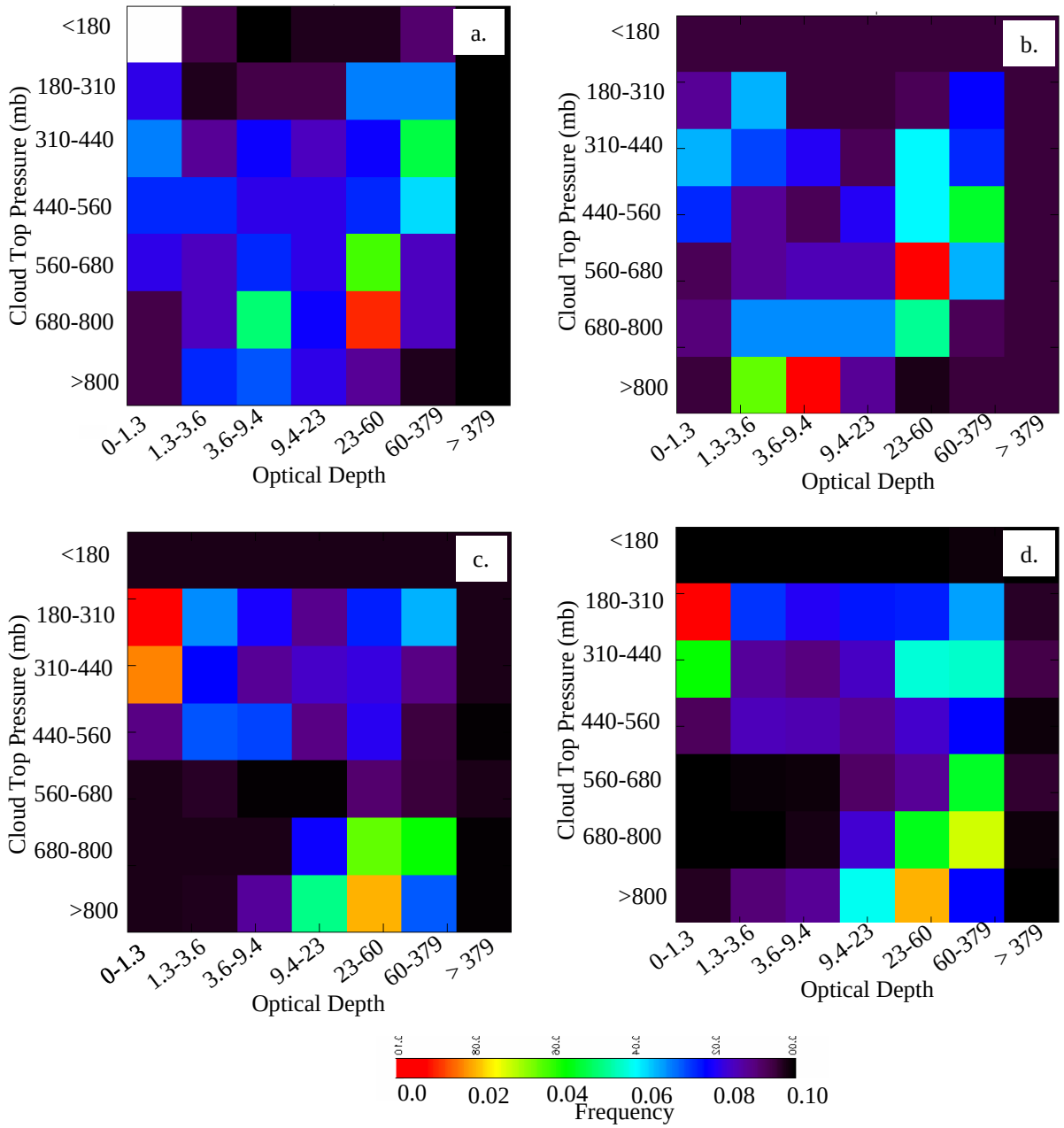

Figure 14. Cloud top pressure and total visible optical depth histograms from a) ISCCP in a 250 km domain centered on the SGP site, b) the nearest pixel of the LBTM algorithm to the ARM SGP site, c) The ARM data CPC diagnostic, and d) the ICARUS simulation of the ISCCP algorithm using the ARM CPC information as input. The period covered is March 2000 during daylight hours.

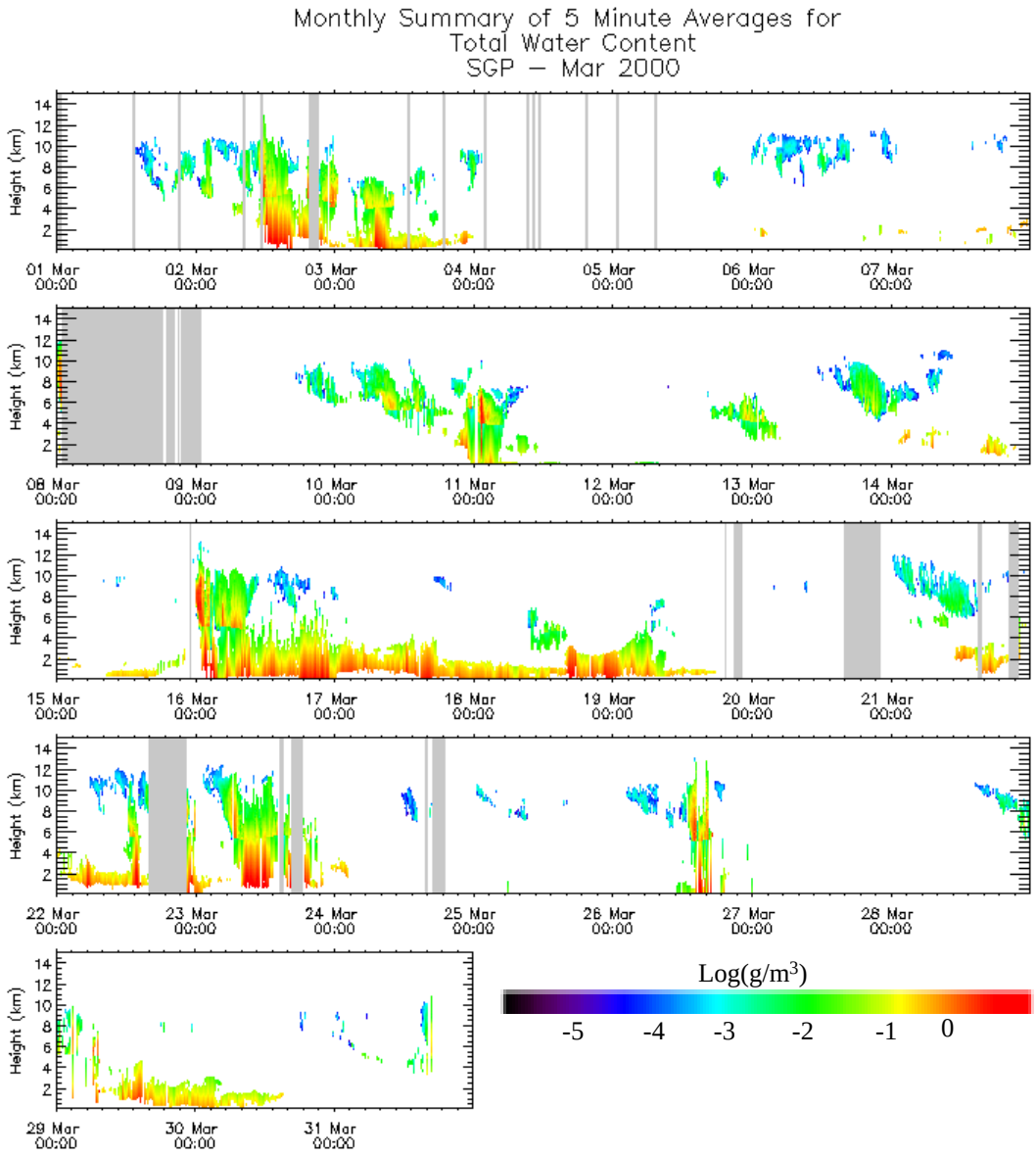
Monthly Summary of 5 Minute Averages for
Total Water Content
SGP – Mar 2000
Height (km)
01 Mar 00:00
02 Mar 00:00
03 Mar 00:00
04 Mar 00:00
05 Mar 00:00
06 Mar 00:00
07 Mar 00:00
08 Mar 00:00
09 Mar 00:00
10 Mar 00:00
11 Mar 00:00
12 Mar 00:00
13 Mar 00:00
14 Mar 00:00
15 Mar 00:00
16 Mar 00:00
17 Mar 00:00
18 Mar 00:00
19 Mar 00:00
20 Mar 00:00
21 Mar 00:00
22 Mar 00:00
23 Mar 00:00
24 Mar 00:00
25 Mar 00:00
26 Mar 00:00
27 Mar 00:00
28 Mar 00:00
29 Mar 00:00
30 Mar 00:00
31 Mar 00:00
Log(g/m3)
-5
-4
-3
-2
-1
0

Figure 15a.

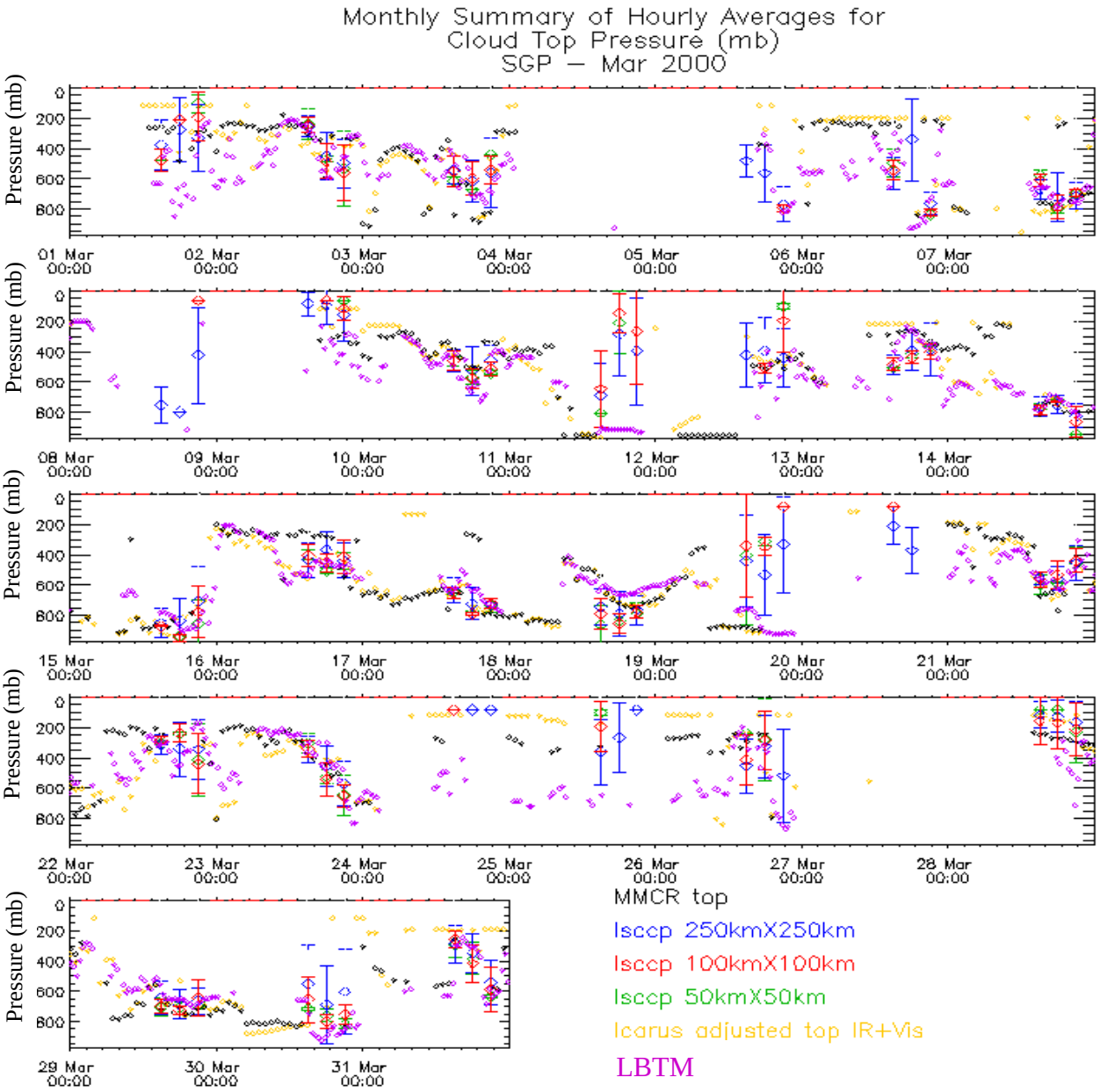
Monthly Summary of Hourly Averages for
Cloud Top Pressure (mb)
SGP – Mar 2000
Pressure (mb)
0
200
400
600
800
01 Mar 00:00
02 Mar 00:00
03 Mar 00:00
04 Mar 00:00
05 Mar 00:00
06 Mar 00:00
07 Mar 00:00
08 Mar 00:00
09 Mar 00:00
10 Mar 00:00
11 Mar 00:00
12 Mar 00:00
13 Mar 00:00
14 Mar 00:00
15 Mar 00:00
16 Mar 00:00
17 Mar 00:00
18 Mar 00:00
19 Mar 00:00
20 Mar 00:00
21 Mar 00:00
22 Mar 00:00
23 Mar 00:00
24 Mar 00:00
25 Mar 00:00
26 Mar 00:00
27 Mar 00:00
28 Mar 00:00
29 Mar 00:00
30 Mar 00:00
31 Mar 00:00
MMCR top
Isccp 250kmX250km
Isccp 100kmX100km
Isccp 50kmX50km
Icarus adjusted top IR+Vis
LBTM

Figure 15b

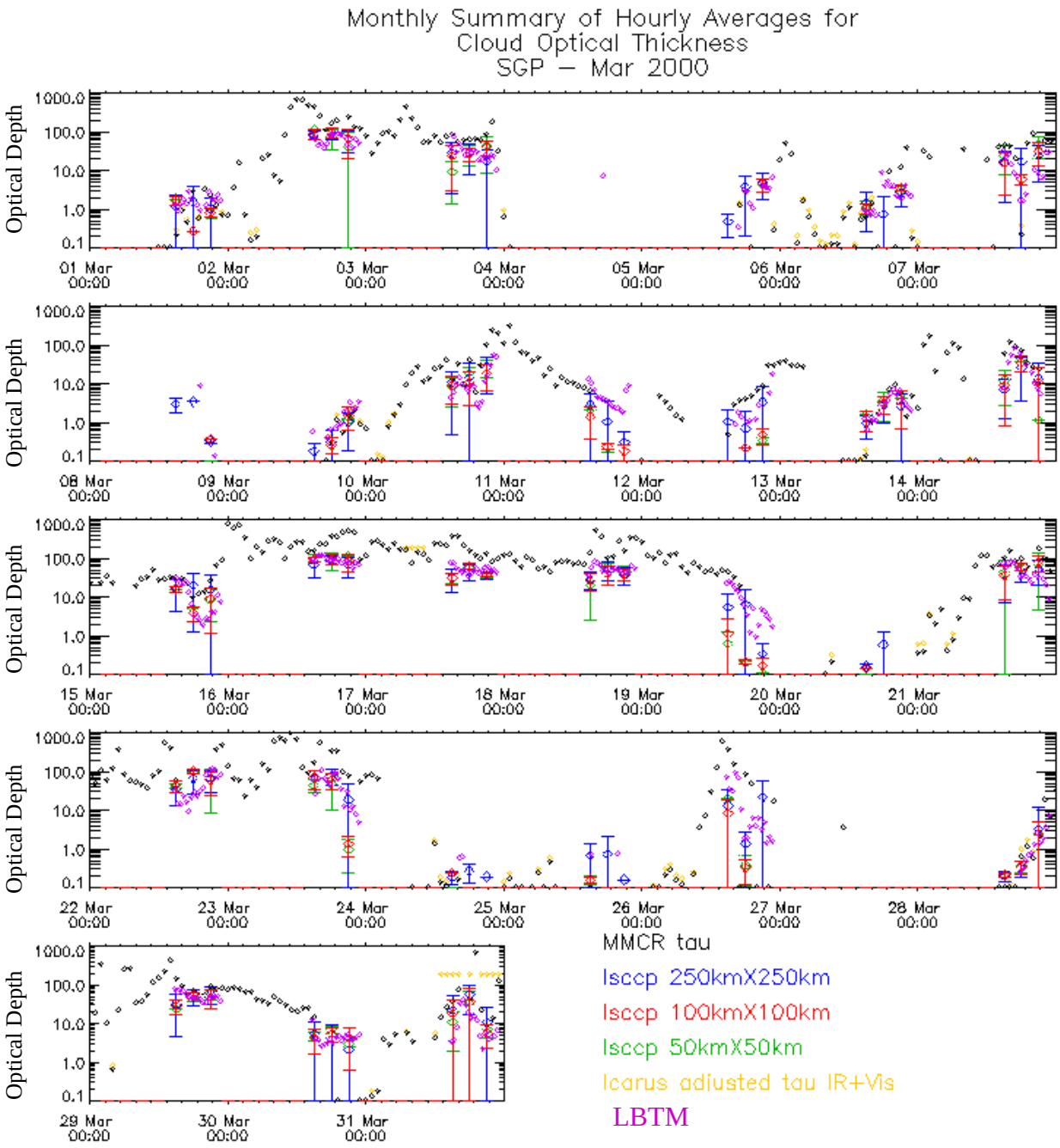

Figure 15. Time series of (a) total condensed water diagnosed using the CPC technique, (b) cloud top pressure and (c) total cloud optical depth during 3/2000 diagnosed from the various sources as shown in the legend. The ISCCP values are shown as means and standard deviations derived in geographic domains centered on the ARM SGP site.

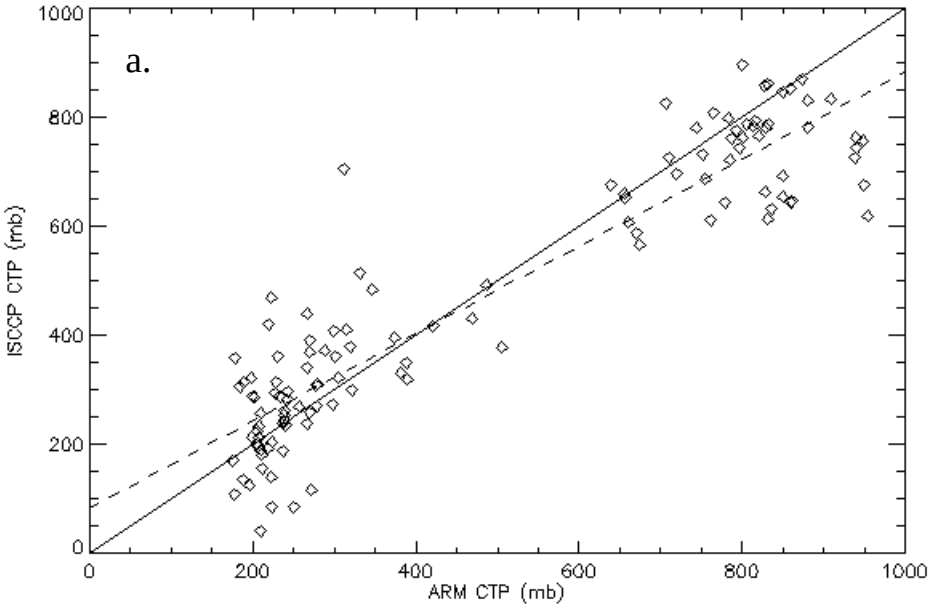

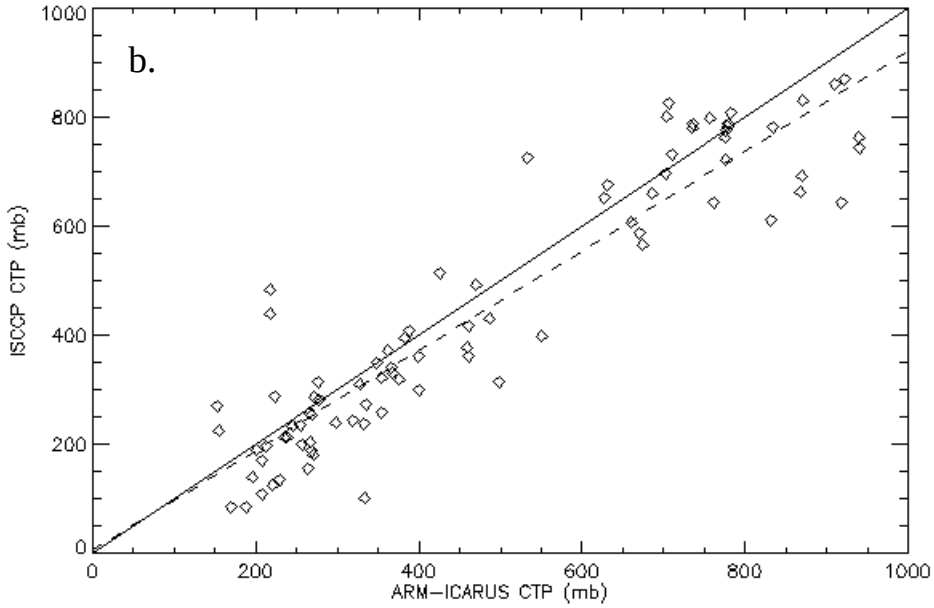

Figure 17a and b

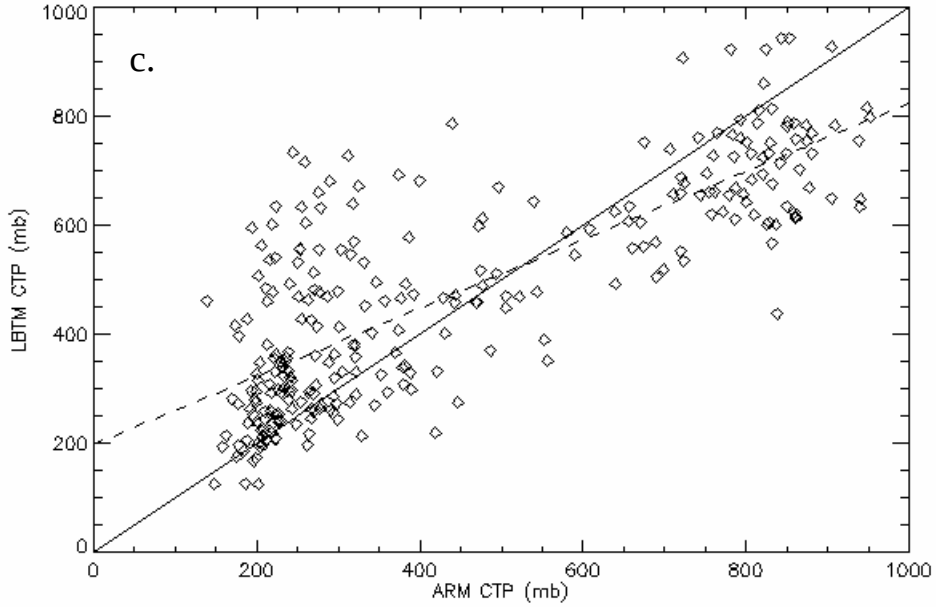

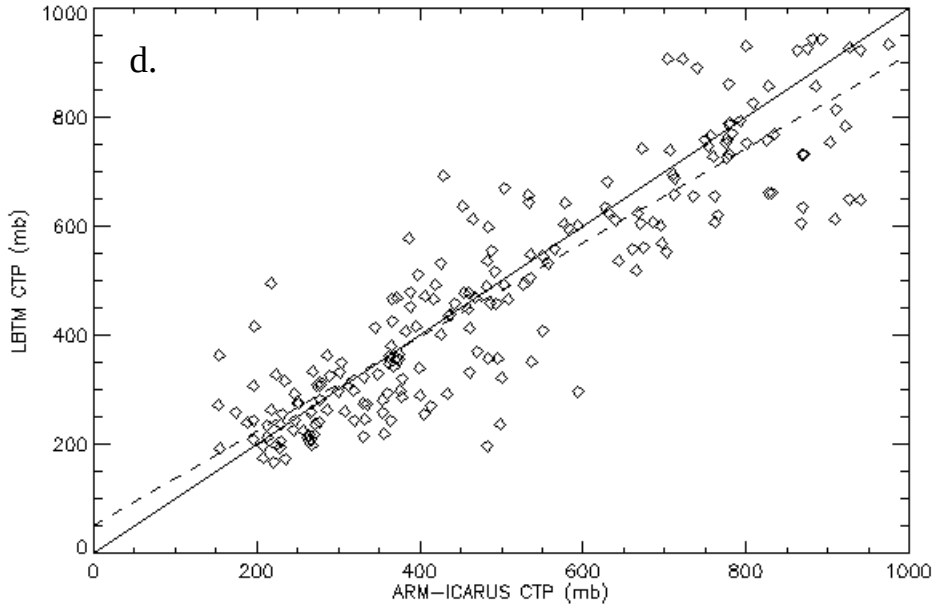

Figure 17c and d

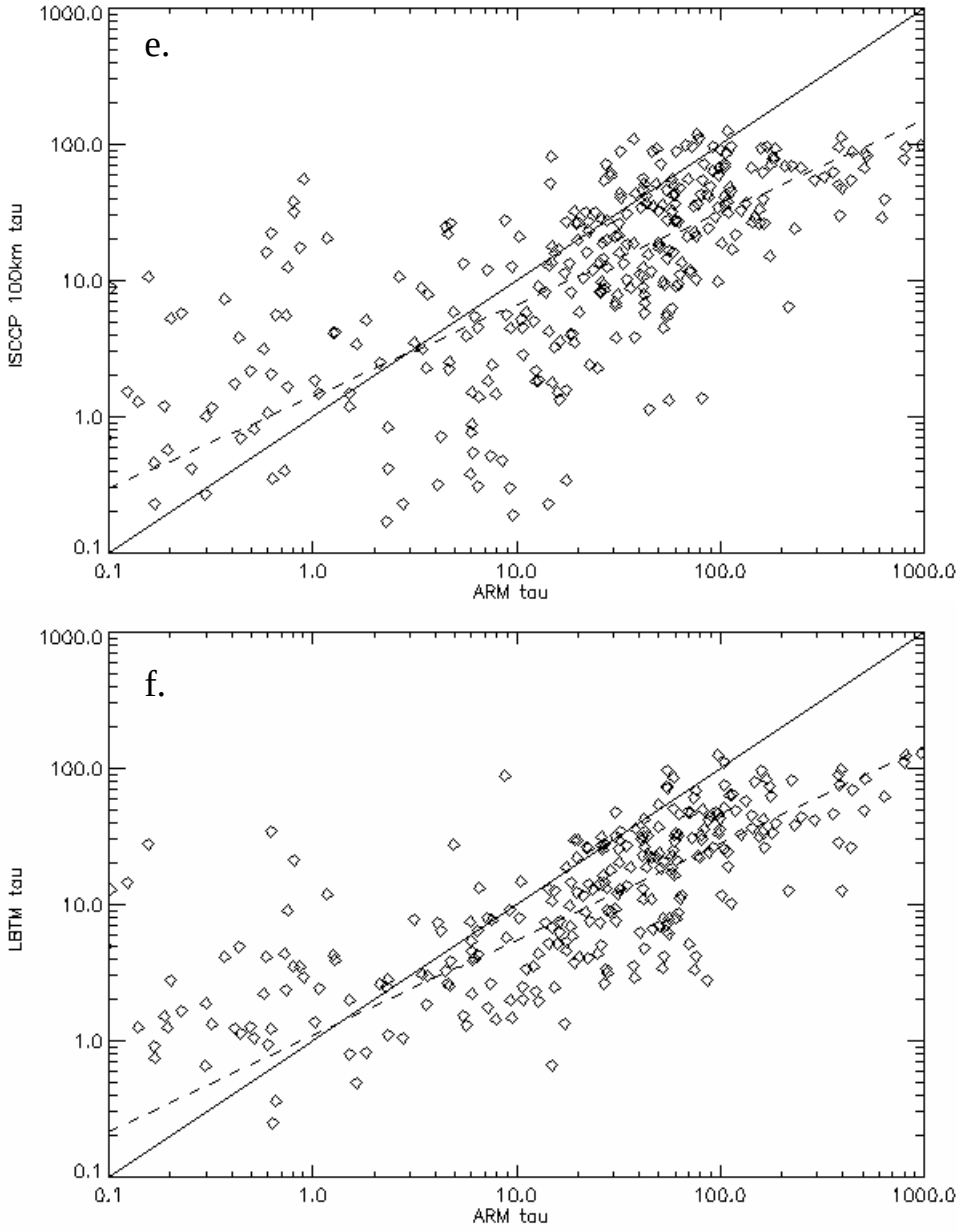

Figure 16. Comparison of ISCCP and LBTM quantities with ARM data. Shown in a) CTP from ISCCP compiled in a 100 km domain centered on the SGP site, b) as in a) except ISCCP is compared with ICARUS simulation using ARM data, c) LBTM from the pixel nearest the ARM SGP site, d) as in c) except LBTM is compared to the ICARUS simulation using ARM data, e) ISCCP optical depth is compared to the quantity derived from the ARM CPC diagnostic and f) as in e) except the Minnis nearest pixel optical depth is compared to ARM.